Title
Coherent x-ray studies of the dynamics of magnetic skyrmions and polymer electrolytes

Author
Holladay, Benjamin William

Publication Date
2019

UNIVERSITY OF CALIFORNIA SAN DIEGO

Coherent x-ray studies of the dynamics of magnetic skyrmions and polymer electrolytes

A dissertation submitted in partial satisfaction of the requirements for the degree

Doctor of Philosophy

in

Physics

by

Benjamin William Holladay

Committee in charge:

Professor Sunil Sinha, Chair
Professor Eric Fullerton
Professor Zhaowei Liu
Professor Brian Maple
Professor Oleg Shpyrko

2019

The dissertation of Benjamin William Holladay is approved, and it is acceptable in quality and form for publication on microfilm and electronically:

Chair

University of California San Diego

2019

TABLE OF CONTENTS

LIST OF FIGURES

ACKNOWLEDGEMENTS

I would like to start by acknowledging by advisor, Professor Sunny Sinha. Sunny and I have worked on a wide variety of experiments using multiple techniques in x-ray and neutron scattering. The nature of synchrotron work leads to long projects that can be difficult for a new graduate student. During my first few years in the group, I struggled with understanding and analyzing the data I had measured. Sunny was endlessly patient and helped me learn how to model and fit my results. When my first set of projects did not prove successful, Sunny helped me learn from my mistakes and gave me new experiments that would ultimately prove the basis for this work. The nature of experimental work is that some experiments fail and Sunny helped me overcome these challenges. He was a huge influence my scientific and professional development and I would not be where I am today without his kind and thoughtful support.

The work presented in this dissertation was highly collaborative and there are dozens of colleagues and collaborators to whom I owe a doubt of thanks. Here I would like to briefly thank some of those people for their support. I would like to thank Dr. Sujoy Roy, Dr. Suresh Narayanan, and all of the other beamline scientists who helped me collect my results. I would like to thank Dr. Matt Seaberg, Dr. Josh Turner, Dr. Sergio Montoya and Prof. Eric Fullerton for all their help with our skyrmion work. I would like to thank Dr. Hans-Georg Steinrück, Dr. Chris Takacs, and Dr. Mike Toney for all of their support on our battery work. I would like to thank Prof. Eric Fullerton, Prof. Zhaowei Liu, Prof. Brian Maple, and Prof. Oleg Shyprko for their advice and support as my thesis committee members.

I would like to thank all of my lab mates, Jing-Jin Song, San-Wen Chen, Yi Yang, Yicong Ma, Sajal Gosh, Hongyu Guo, Sambunath Bera, Rupak Bhattachargya, and Sudip

Pandey, who made it a pleasure to come to work and whose help through many experiments is greatly appreciated.

I would like to thank all of friends who have supported and believed in me over this long journey to finishing by Ph.D, especially, Jamie Wampler, Ilya Valmianski, and Daniel Johnson. Without their friendship, encouragement, levity, and advice, graduate school would have been a significantly worse experience that I'm not sure I would have finished.

Finally, I would like to thank my family. I would like to thank my parents, Ken and Wendy. They always believed in me and where always there for me through my darkest moments. No matter how much complaining I did, they always tried to brighten my mood. I would also like to thank my siblings, Annie, Rachel, and Sam. I cannot imagine my life without them. Through our shared experiences, they have been comrades in this long winding journey to getting my Ph.D. And while graduate school was usually a deeply frustrating endeavor, the time away from school that I spent with my family made it all worthwhile. I love you all.

I gratefully acknowledge the funding source that supported my Ph.D. work at UCSD. I was funded by grant number DE-SC0003678 from the Division of Basic Energy Science, U.S. Dept. of Energy.

The text in Chapter 4 is based on material published in

M. H. Seaberg, B. Holladay, J. C. T. Lee, M. Sikorski, A. H. Reid, S. A. Montoya, G. L. Dakovski, J. D. Koralek, G. Coslovich, S. Moeller, W. F. Schlotter, R. Streubel, S. D. Kevan, P. Fischer, E. E. Fullerton, J. L. Turner, F.-J. Decker, S. K. Sinha, S. Roy, J. J. Turner. Nanosecond x-ray photon correlation spectroscopy on magnetic skyrmions. *Phys. Rev. Lett.* 119, 67403 (2017). The dissertation author was a major contributor to this paper.

The text in Chapter 4 is based on material that has been submitted for publication in

M. H. Seaberg, B. Holladay, X. Y. Zheng, J. C. T. Lee, A. H. Reid, S. A. Montoya, J. D. Koralek, G. Coslovich, P. Walter, S. Zohar, V. Thampy, M. F. Lin, P. Hart, K. Nakahara, R. Steubel, S. D. Kevan, P. Fischer, W. Colocho, A. Lutman, F.-J. Decker, E. E. Fullerton, M. Dunne, S. Roy, S. K. Sinha, J. J. Turner. Magnetic Skyrmion Fluctuations. Submitted. The dissertation author was a major contributor to this paper.

The text in Chapter 5 is based on material prepared for submission by

H. G. Steinruck, B. Holladay, C. Takacs, D. Mackanic, H. K. Kim, C. Cao, S. Narayanan, E. Dufresne, Y. Chushkin, B. Ruta, F. Zontone, J. Will, O. Borodin, S. K. Sinha, V. Srinivasan, M. Toney. “Understanding ion transport in polymeric electrolytes via x-ray photon correlation spectroscopy”. The dissertation author was a major contributor to this paper.

VITA

2010	Bachelor of Science in Physics, Georgia Institute of Technology
2019	Doctor of Philosophy in Physics, University of California, San Diego

PUBLICATIONS

M. H. Seaberg, **B. Holladay**, J. C. T. Lee, M. Sikorski, A. H. Reid, S. A. Montoya, G. L. Dakovski, J. D. Koralek, G. Coslovich, S. Moeller, W. F. Schlotter, R. Streubel, S. D. Kevan, P. Fischer, E. E. Fullerton, J. L. Turner, F.-J. Decker, S. K. Sinha, S. Roy, J. J. Turner. Nanosecond x-ray photon correlation spectroscopy on magnetic skyrmions. *Phys. Rev. Lett.* 119, 67403 (2017)

M. H. Seaberg, **B. Holladay**, X. Y. Zheng, J. C. T. Lee, A. H. Reid, S. A. Montoya, J. D. Koralek, G. Coslovich, P. Walter, S. Zohar, V. Thampy, M. F. Lin, P. Hart, K. Nakahara, R. Steubel, S. D. Kevan, P. Fischer, W. Colocho, A. Lutman, F.-J. Decker, E. E. Fullerton, M. Dunne, S. Roy, S. K. Sinha, J. J. Turner. Magnetic Skyrmion Fluctuations. Submitted.

H. G. Steinruck, **B. Holladay,** C. Takacs, D. Mackanic, H. K. Kim, C. Cao, S. Narayanan, E. Dufresne, Y. Chushkin, B. Ruta, F. Zontone, J. Will, O. Borodin, S. K. Sinha, V. Srinivasan, M. Toney. Understanding ion transport in polymeric electrolytes via x-ray photon correlation spectroscopy. In preparation

T. O. Farmer, E. J. Guo, R. D. Desautels, L. DeBeer-Schimitt, A. Chen, Z. Wang, Q. Jia, J. A. Borchers, D. A. Gilber, **B. Holladay**, S. K. Sinha, M. R. Fitzsimmons. Nanoscale magnetization inhomogeneity within single phase nanopillars. *Phys. Rev. Mater.* 3, 081401 (2019)

ABSTRACT OF THE DISSERTATION

Coherent x-ray studies of the dynamics of magnetic skyrmions and polymer electrolytes

by

Benjamin William Holladay

Doctor of Philosophy in Physics

University of California San Diego, 2019

Professor Sunil K. Sinha, Chair

The use of coherent x-rays has grown recently with the development of high brilliance x-ray sources. X-ray photon correlation spectroscopy (XPCS) has proven to be a valuable tool to measure the dynamics of a wide range of systems. In this dissertation we utilized two extensions to the standard XPCS method. The first is called two-pulse XPCS. By measuring the speckle pattern from the two x-ray pulses separated in time, we can measure the dynamics of systems at much shorter time scales than conventional XPCS. To demonstrate the viability of this technique, we measured the equilibrium fluctuations of a magnetic skyrmion lattice in a FeGd multiplayer. These results showed an exponential decay in the intermediate scattering function and gave valuable insight into the dynamics of the creation and decay of the skyrmion lattice.

They also demonstrated the viability of the two-pulse technique as a potential method to measure ultrafast dynamics using coherent x-rays. The second is heterodyne XPCS. This method involves interfering the sample's scattering with a static reference signal. This interference allows the measurement of a uniform flow of scatterers. Using this technique, we have directly measured the velocity of ions inside a polymer electrolyte under an applied voltage. These results show the correlation between the ion's velocity and the output current of the cell. There is an initial spike in the ion's velocity as the voltage is first applied. Then an internal concentration gradient forms and the velocity decays to steady state. We show how this velocity is dependent on the applied voltage and temperature of the system. The concentration gradient is directly measured and compared with the velocity measured using heterodyne XPCS. The direct measurement of the ion's velocity and concentration in-situ are the first of their kind for a polymer electrolyte. They provide valuable data about the transference number of the system.

Chapter 1. Introduction

X-ray scattering offers a flexible set of tools to nondestructively probe the structural and dynamical properties of a wide variety of materials. They are typically used to carry out diffraction, reflectometry, and small angle scattering. These techniques provide excellent tools to measure the structure at nanometer length scales and have found widespread adoption. The invention of high brilliance coherent x-ray sources and high-speed x-ray detectors have expanded the capabilities of x-ray scattering to measure time dynamics. By utilizing coherent x-rays, we can measure the dynamics of a systems with time scales from nanoseconds to hundreds of seconds. The high penetration depth of x-ray and small focus size constitute a highly localized probe to measure the dynamics in a wide variety of systems. These capabilities have been greatly enhanced by third generation synchrotron sources whose high brilliance means weaker effects can be studied. This can be used on complex objects, such as batteries *in-situ* to understand their internal transport and dynamics. In addition, when an x-ray photon interacts resonantly with an atom, it can reveal information about the magnetic properties of a system. This makes x-rays an excellent tool for understanding complex magnetic phenomena.

This dissertation explains how we used x-ray photon correlation spectroscopy (XPCS) to study the dynamics and transport of several materials, including magnetic skyrmions in a multilayer and battery polymer electrolytes. This thesis is structured as follows. Chapter 2 includes a brief review of the scientific background of x-ray scattering. First, the interaction between x-rays and matter. Then resonant magnetic x-ray scattering. Followed by the basics of coherence and speckle. Finally, an overview of standard XPCS theory. Chapter 3 describes the theory of two-pulse XPCS and magnetic skyrmions. Two-pulse XPCS is a novel extension of standard XPCS that enables us to measure dynamics much faster than the standard method by decoupling the time scale from the speed of the detector. We used this new technique to measure the dynamics of magnetic skyrmions in a FeGd multilayer. A brief treatment of the theory of magnetic skyrmions is included. Chapter 4 covers the results of our two-pulse XPCS measures on FeGd. The results of two separate experiments will be presented. The first experiment primarily demonstrated the viability of the technique. The second experiment extended results of the first measurement to include more delay times, magnetic fields, and speckle patterns to improve our understanding of the dynamics of the skyrmion system. Chapter 5 discusses the results of our heterodyne XPCS measurements on polymer electrolytes. First, an introduction to polymer electrolytes is presented. Then an explanation of the methods including heterodyne XPCS and x-ray absorption is given. Finally, the results show the measured ion velocity and concentration at multiple temperatures under applied voltage. This provides the first experimental measurement of ion velocity in a polymer electrolyte.

Chapter 2. X-ray interactions with matter

In the following chapter, the basic principles of x-ray scattering will be discussed. A particular emphasis will be placed on coherence and its application to measure dynamical properties using x-ray photon correlation spectroscopy (XPCS).

2.1. X-ray scattering

X-ray scattering encompasses a wide range of techniques that are used to probe the structural and dynamical properties of atomic and nanoscale systems. X-rays are defined as electromagnetic radiation with a wavelength between 0.01 nm and 10 nm. It is this wavelength that allows x-rays to interact with the nanostructure of complex systems. X-ray photons with relatively low energy, below 2 keV, are known as soft x-rays, while x-rays with energy greater than 5 keV are known as hard x-rays. The lower energy of soft x-ray photons allows them to match the lower energy magnetic resonances of transition metals and rare earth metals. This gives soft x-rays the unique ability to probe the magnetic structure of materials. Unfortunately, the lower energy means they are absorbed by most substances and this makes experimental design difficult. Furthermore, their lower energy means they have a lower penetration depth. The much higher energy of hard x-rays gives them a much greater penetration depth and their lower absorption means they can be used outside of a vacuum chamber. Because of this ease of use, they are the preferred method of measuring the bulk properties of systems techniques like diffraction and reflectivity [1, 2]. X-rays can interact with matter in two ways, scattering or absorption. Is this work, we are mainly interested in the dynamical properties of materials measured with scattering.

The simplest interaction between an x-ray photon and electron is through charge scattering [3]. This interaction can be modeled using classical electrodynamics where the oscillating electric field of an x-ray photon, modeled as a plane wave with a single frequency, causes the electron to vibrate in the direction of the electric field. The vibration of a charged particle then causes the electron to reradiate a scattered photon of the same energy as a spherical wave (E_{rad}), whose polarization depends on the incident beam. For synchrotron radiation the incident beam usually has horizontal polarization. This phenomenon is known as Thomson scattering [4]. In the far-field limit, the electric field is given by:

$$|E_{rad}|^2 = |E_{in}|^2 \left(\frac{r_0^2}{R^2}\right) P \tag{2.1}$$

where r_0 the classical radius of the electron and P is the polarization factor of scattering defined as 1 for vertical scattering plane and $cos^2\, 2\theta$ for horizontal scattering plane where 2θ is the scattering angle of the detector from the incident beam direction.

In our scattering experiments, the physical quantity measured by the detector is the differential scattering cross-section, which is defined as the scattering intensity normalized by the incident flux I_0 where the detector subtends solid angle $\Delta\, \Omega$

$$\frac{d\,\sigma}{d\,\Omega} = \frac{\#\ of\ photons\ scattered\ per\ sec\ into\ \Delta\,\Omega}{I_0\ \times\ \Delta\,\Omega} = \frac{|E_{rad}|^2\ R^2}{|E_{in}|^2} \tag{2.2}$$

Using equation 2.1 we get the differential scattering cross-section for an electron from Thomson scattering:

$$\frac{d\,\sigma}{d\,\Omega} = r_0^2\ P \tag{2.3}$$

To understand scattering from an atom, we model it as a collection of Z electrons distributed with number density $\rho(\boldsymbol{r})$. Taking the superposition, we find the phase difference

$$\Delta\phi(\boldsymbol{r}) = \left(\boldsymbol{k}_f - \boldsymbol{k}_i\right) \cdot \boldsymbol{r} = \boldsymbol{Q} \cdot \boldsymbol{r} \tag{2.4}$$

where $\boldsymbol{k}_f$ and $\boldsymbol{k}_i$ are the scattered and incident wave vectors respectively and $\boldsymbol{Q}$ is the momentum transfer vector or scattering vector $(\boldsymbol{k}_f - \boldsymbol{k}_i)$. Using the phase of the scattering vector, we can calculate the total scattering length from the atom as the Fourier transform of the electron density $\rho(\boldsymbol{r})$.

$$f^0(\boldsymbol{Q}) = \int \rho(\boldsymbol{r})\, e^{i\,\boldsymbol{Q}\cdot\boldsymbol{r}}\, d\boldsymbol{r} \tag{2.5}$$

where $f^0(\boldsymbol{Q})$ is called the atomic form factor. With scattering vector of 0, this reduces to Z, the total number of electrons. For nonzero $\mathbf{Q}$, quantum mechanics are required to evaluate the electron density and calculate the atomic form factor. This approximation has neglected any dispersive or absorptive effects. To incorporate these effects, we must add a frequency dependent term for each given by quantum mechanics.

$$f(\boldsymbol{Q}, \omega) = f^0(\boldsymbol{Q}) + f'(\omega) + i\, f''(\omega) \tag{2.6}$$

These terms are small away from absorption edges. However, near the resonant edge of a particular element, the absorption term can become strong.

The scattering from a collection of atoms is built up in a similar way to the scattering from multiple electrons around one atom. It is expressed in terms of the scattering vector

$$|\boldsymbol{Q}| = \frac{4\pi}{\lambda} \sin\theta \tag{2.7}$$

where θ is the scattering angle and λ is the x-ray wavelength. The length scale (L) being measured in the experiment is given by $L = 2\pi/|\boldsymbol{Q}|$. For small angle transmission experiments, like the ones presented in the later chapters, these length scales are between 10 nm and 100 nm.

The scattering amplitude, $F(\boldsymbol{Q})$, can be written as a sum of the scattering from each atom as follows:

$$F(\boldsymbol{Q}) = \sum_i f_i^0(\boldsymbol{Q}) e^{i\boldsymbol{Q}\cdot\boldsymbol{r}_i} \tag{2.8}$$

where $\boldsymbol{r_i}$ are the position of each atom and f_i^0 is the atomic form factor for each atom. The scattered intensity is given by

$$I(\boldsymbol{Q}) = |F(\boldsymbol{Q})|^2 = \sum_{i,j} f_i^0(\boldsymbol{Q}) f_j^{0*}(\boldsymbol{Q}) e^{i\boldsymbol{Q}\cdot\boldsymbol{r}_i} e^{-i\boldsymbol{Q}\cdot\boldsymbol{r}_j} \tag{2.9}$$

This sum can easily be expressed as an integral for a continuous electron density as follows

$$I(\boldsymbol{Q}) = |f^0(\boldsymbol{Q})|^2 \iint \langle \rho(\boldsymbol{r}_i)\rho(\boldsymbol{r}_j)\rangle \, e^{i\,\boldsymbol{Q}\cdot(\boldsymbol{r}_i-\boldsymbol{r}_j)} d\boldsymbol{r}_i d\boldsymbol{r}_j \tag{2.10}$$

where $\rho(\boldsymbol{r_i})$ is the electron density in volume element dr_i and the time average is taken over the detection interval. This gives the scattering intensity for a collection of atoms as the Fourier transform of their electron density.

2.2. Resonant magnetic scattering

In addition to charge scattering described above, x-rays can also interact with the magnetism of a sample. Far away from resonances this scattering is very weak, of the order of 10^{-4} of the charge scattering. However, for photon energies in the vicinity of the L-M-absorption edge of a magnetic atom, the resonant magnetic scattering become very large and can be comparable to or even larger than the charge scattering [5]. Thus, we add a magnetic term to the atomic form factor

$$f(\boldsymbol{Q},\omega) = f^0(\boldsymbol{Q}) + f'(\omega) + i\,f''(\omega) + f_{mag}(\boldsymbol{Q},\omega) \tag{2.11}$$

This magnetic term will depend on the resonant energy of the atom [6]. In quantum mechanics, the electrons of every atom occupy discrete energy levels. The energy difference between these levels is called its resonant energy. By matching the x-ray energy to this resonant energy, we can induce transitions in the atom and greatly enhance the scattering. The most intense transition is called the electric dipole transition, E1. To measure the magnetic state of the system, the electric dipole transition must excite an electron into the atom's magnetic orbitals. For Gadolinium, this transition is from $3d \rightarrow 4f$ and is called the Gd M_5 edge. It has an energy of 1192 eV. For elastic scattering, the scattering amplitude for the transition is given by [7]

$$f_{E1}\left(\boldsymbol{k}_f, \boldsymbol{k}_i, \omega\right) = \frac{4\pi}{r_0 k} \sum_{M=-1}^{+1} \left(\boldsymbol{e}_f^* \cdot \boldsymbol{Y}_{1M}^{(e)}\left(\widehat{\boldsymbol{k}}_f\right) \boldsymbol{Y}_{1M}^{(e)*}\left(\widehat{\boldsymbol{k}}_i\right) \cdot \boldsymbol{e}_i\right) F_{1M}^{(e)}(\omega) \qquad (2.12)$$

Where $\boldsymbol{Y}_{1M}^{(e)}$ is the vector spherical harmonic, $\boldsymbol{e_f}, \boldsymbol{e_i}$ are the unit polarization vectors, and $F_{1M}^{(e)}$ is the transition matrix element. The matrix element is determined by the probability of the initial and final states and the transition energy as follows

$$F_{1M}^{(e)}(\omega) = \sum_{\alpha,\eta} \left(\frac{p_\alpha p_\alpha(\eta) \Gamma_x(\alpha M \eta)/\Gamma(\eta)}{x(\alpha,\eta) - i} \right) \qquad (2.13)$$

where p_α is the probability for the atom to be in the initial state $|\alpha\rangle$, $|\eta\rangle$ is the excited state, $p_\alpha(\eta)$ being the probability that the state is vacant for the transition from $|\alpha\rangle$, Γ_x gives the partial line width for the E1 radiative decay, and $\Gamma(\eta)$ is the total width for the excited state. The denominator $x(\alpha,\eta) = (E_\eta - E_\alpha - \hbar\omega)/(\Gamma(\eta)/2)$ is the deviation from resonance in units of $\Gamma(\eta)/2$. For photon energy $\hbar\omega = E_\eta - E_\alpha$, this term becomes very large giving a large enhancement to the scattering. The polarization dependence is determined by the vector spherical harmonics. For the electric dipole transition we have

$$\left(\boldsymbol{e}_f^* \cdot \boldsymbol{Y}_{1\pm1}^{(e)}(\widehat{\boldsymbol{k}}_f)\boldsymbol{Y}_{1\pm1}^{(e)*}(\widehat{\boldsymbol{k}}_i) \cdot \boldsymbol{e}_i\right) = \left(\frac{3}{16\pi}\right)\left[\boldsymbol{e}_f^* \cdot \boldsymbol{e}_i \mp i\left(\boldsymbol{e}_f^* \times \boldsymbol{e}_i\right) \cdot \hat{\boldsymbol{z}} - (\boldsymbol{e}_f^* \cdot \hat{\boldsymbol{z}})(\boldsymbol{e}_i \cdot \hat{\boldsymbol{z}})\right] \tag{2.14}$$

$$\left(\boldsymbol{e}_f^* \cdot \boldsymbol{Y}_{10}^{(e)}(\widehat{\boldsymbol{k}}_f)\boldsymbol{Y}_{10}^{(e)*}(\widehat{\boldsymbol{k}}_i) \cdot \boldsymbol{e}_i\right) = \left(\frac{3}{16\pi}\right)\left[(\boldsymbol{e}_f^* \cdot \hat{\boldsymbol{z}})(\boldsymbol{e}_i \cdot \hat{\boldsymbol{z}})\right] \tag{2.15}$$

where $\hat{\boldsymbol{z}}$ is the unit magnetization vector. Combining these expressions gives a final scattering amplitude for the electric dipole transition as

$$\begin{aligned} f_{E1}(\boldsymbol{k}_f, \boldsymbol{k}_i, \omega) = \frac{3}{4k}\Big\{&\left(\boldsymbol{e}_f^* \cdot \boldsymbol{e}_i\right)\left[[F_{11}^{(e)} + F_{1-1}^{(e)}\right] - i\left(\boldsymbol{e}_f^* \times \boldsymbol{e}_i\right) \cdot \hat{\boldsymbol{z}}\left[[F_{11}^{(e)} - F_{1-1}^{(e)}\right] \\ &+ (\boldsymbol{e}_f^* \cdot \hat{\boldsymbol{z}})(\boldsymbol{e}_i \cdot \hat{\boldsymbol{z}})\left[2F_{10}^{(e)} - F_{11}^{(e)} - F_{1-1}^{(e)}\right]\Big\} \end{aligned} \tag{2.16}$$

The first term has no dependence on the magnetization and gives the resonant enhancement in charge scattering. The second term depends linearly on the sample magnetization and is used in x-ray magnetic circular dichroism. The third term depends quadratically on magnetization and gives rise to second harmonic magnetic peaks and is used in x-ray linear dichroism [8].

2.3. Coherence and speckle

The assumption from the previous section of a monochromatic plane wave can be generalized for multiple photons as coherent flux. A coherent x-ray beam would have all the photons with the same energy, phase, and direction. For realistic x-ray sources this requirement is relaxed slightly to allow small variation in these properties. For many years, these requirements were impossible to meet with available x-ray sources with earlier synchrotrons having a very low fraction of their total intensity as coherent flux. Recently, third generation x-ray synchrotron sources have advanced enough to offer usable coherent flux for a wide range of systems. Finally, new x-ray free electron lasers, such as the LCLS at SLAC, can provide high brilliance fully coherent x-ray beams that we utilize to push the limits of coherent scattering [9].

Given the challenges of creating coherent x-ray sources, realistic experimental design must be prepared to deal with only partially coherent beams with a spread of energies. Energy uniformity is typically achieved through the use of monochromators after the x-ray generation to ensure a narrow energy bandwidth. This is usually discussed as the range of energies produced $(\Delta\lambda)$ normalized by the average energy (λ), where $\Delta\lambda/\lambda \sim 0.1\%$ is a typical figure. Second, the spatial uniformity of the beam will be imperfect. To quantify this, we use the coherence lengths

$$L_l = \frac{\lambda^2}{2\,\Delta\lambda}$$

$$L_t = \frac{\lambda}{2}\left(\frac{\mathrm{L}}{d}\right) \tag{2.17}$$

where L_l is the longitudinal coherence length, L_t is the transverse coherence length, L is the distance between the x-ray source and the sample, and d is the lateral size of the source [10]. This gives an overall coherence volume that scales with λ^3 making coherent x-ray experiments considerably harder than visible light. For APS, a typical third generation synchrotron where we performed some of the experiments, the energy bandwidth is 0.1 %, the longitudinal coherence length is around 1 micron, and the transverse coherence length is between 2 and 150 microns.

In addition to coherence volume, the overall intensity is of critical importance. The coherent flux is defined as:

$$I_{coherent} = \frac{B\,\sigma_x\,\sigma_y\,L_x L_y}{R^2} = \frac{B\,\lambda^2}{4} \tag{2.18}$$

where B is the number of photons per second per unit area per solid angle, typically called brilliance. At APS, $B > 10^{20}$ giving a coherent intensity of $I_c \approx 10^{10}$ photons per second. This shows the large tradeoff required to perform coherent measurements and the importance of high brilliance sources. In addition, new x-ray free electron lasers show even higher brilliance and longer coherence lengths enabling a whole new class of experiments.

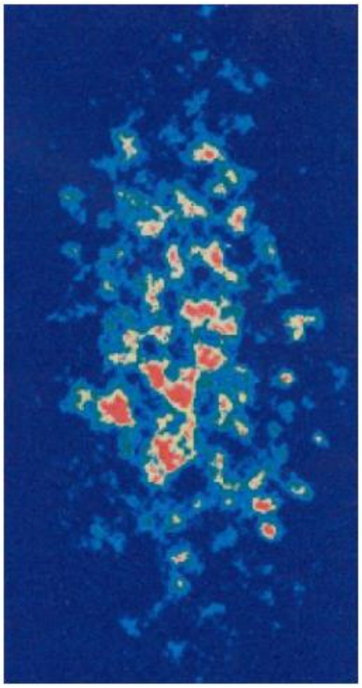

Figure 2.1: First observed x-ray speckle pattern from a superlattice peak of Cu_3Au [11].

In visible light, the effect of coherent scattering results in a speckle pattern (see Figure 2.1). This random intensity pattern is the result of random scatters illuminated in the coherence volume producing random phases that interfere to produce a speckle pattern. As shown from the scattering expression above, this random speckle pattern corresponds to the particular position of the atoms in the system. It is a unique fingerprint of the structure of the sample. Any change in the configuration of the sample will produce a different speckle pattern even if the average properties of the system remain the same. However, fluctuations larger than the coherence length will not be resolved by the measurement. Finally, all experimental techniques utilizing coherence have been performed with partially coherent beams, the theoretical treatment of which is beyond the scope of this work [12, 13]. The first x-ray speckle pattern was measured from randomly arranged domains in a single crystal of Cu_3Au [11] and has been observed in magnetic systems [14] and charge density waves in Cr [15].

2.4. X-ray Photon Correlation Spectroscopy (XPCS)

One technique that utilizes the coherent properties described above is x-ray photon correlation spectroscopy (XPCS). In this method, the goal is to the measure the time-dependent fluctuations in the sample by observing the speckle at a particular scattering vector $(\boldsymbol{Q})$ at different times and taking correlation functions between successive scattering patterns. This allows us to measure the dynamics of a system at a particular length scale $2\pi/|\boldsymbol{Q}|$ and for any time scale that is slower than measurement time of our detectors. In visible light scattering, this technique is called dynamical light scattering and typically employs a laser to provide the coherent flux [16]. XPCS is the x-ray equivalent; however, the smaller wavelength of x-rays means that XPCS can be used to probe much smaller length scales. The time scales available to XPCS have traditionally been limited by the speed of x-ray detectors, although we shall show later on that the novel technique we developed have enabled us to extend this down to the nanosecond regime. Furthermore, resonant XPCS can also be employed to measure the dynamics of a magnetic system. These time and length scale capabilities complement existing neutron scattering techniques, like neutron spin echo as shown in Figure 2.2 [17].

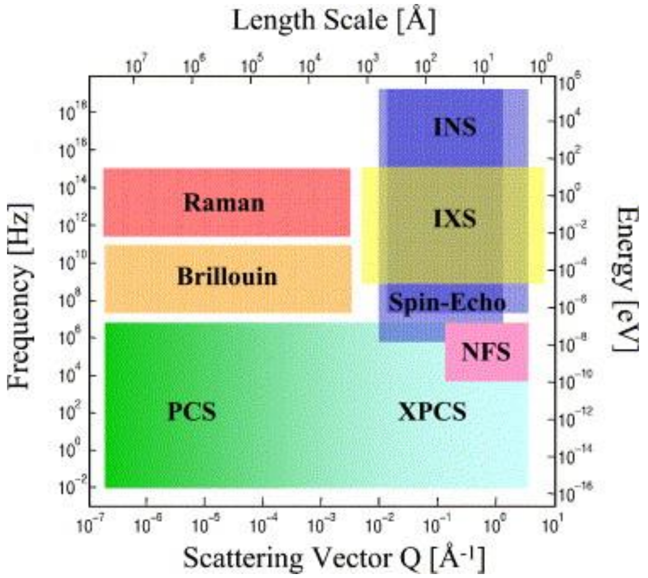

Figure 2.2: Time and length scale covered by XPCS compared to other scattering techniques [17].

The most basic XPCS experiment involves measuring a series of speckle scattering patterns on an area detector as a function of time. Using these scattering patterns, a temporal autocorrelation function is then calculated as follows;

$$g_2(\boldsymbol{Q},\tau) = \frac{\langle I(\boldsymbol{Q},t)\, I(\boldsymbol{Q},t+\tau)\rangle_t}{\langle I(\boldsymbol{Q},t)\rangle_t^2} \tag{2.19}$$

where τ is the delay time and $\langle\ldots\rangle_t$ time average is taken over the entire measurement run [18]. Care must be taken when calculating this time average if the overall intensity of the incoming beam fluctuates [14]. Assuming the electric fields are random Gaussians, the time autocorrelation function is related to the first order correlation function by the Siegert relation [16]

$$g_2(\boldsymbol{Q},\tau) = 1 + \beta(\boldsymbol{Q})|g_1(\boldsymbol{Q},\tau)|^2 \tag{2.20}$$

where $\beta(\boldsymbol{q})$ is the experimental contrast. This contrast depends on the coherence volume, scattering intensity, and detector parameters and would be unity for a fully coherent beam.

Typical synchrotron experiments, like the ones referenced in the following chapters, have a contrast around 10% [19]. $g_1(\mathbf{Q}, \tau)$ is the density-density correlation function, also called the normalized intermediate scattering function

$$g_1(\boldsymbol{Q}, \tau) = \frac{F(\boldsymbol{Q}, \tau)}{F(\boldsymbol{Q}, 0)} \tag{2.21}$$

with the structure factor defined as

$$F(\boldsymbol{Q}, \tau) = \frac{1}{N\langle b \rangle^2} \sum_{n,m}^{N} \langle \mathrm{b_n\ b_m} * \exp(i\boldsymbol{Q} \cdot [\boldsymbol{r}_n(0) - \boldsymbol{r}_m(\tau)]) \rangle \tag{2.22}$$

where $\boldsymbol{r}_n(\tau)$ is the position of particle n at time τ, b_n is the scattering length of particle n, and the brackets denote an ensemble average. For simple systems undergoing diffusive Brownian motion $g_2(\boldsymbol{Q}, \tau)$ can be fit with an exponential decay function [20]. For more complex heterodyne systems, where the scattering signal from the sample is made to interfere with a static reference signal, oscillations occur and a more complex fitting procedure described later will be required that will be discussed in a later chapter [21].

Chapter 3. Theory of magnetic skyrmions and two-pulse XPCS

3.1. Introduction

While XPCS is a useful tool for measuring the dynamics of a wide variety of systems with nanometer length scales, its time resolution is currently limited by the speed of the x-ray detectors. Due to the technology of current x-ray detectors, reading out a large area detector is a relatively slow process. Even the fastest detectors are limited to the order of tens of microseconds, and can easily take much longer if a large area is being measured [22]. We performed a novel variation on XPCS utilizing a two-pulse technique to extend the temporal resolution down to the nanosecond time scale. Instead of measuring a series of speckle patterns repeatedly in time and computing correlation functions of these images, we utilized the statistical properties of optical speckle to measure their contrast. By having a fixed delay time between a pair of coherent x-ray pulses and measuring the probability distribution of their speckle patterns, we can obtain their speckle contrast. Then, by varying the delay time between pulses, we can map out the scattering function as a function of time. With this novel capability, we have measured the intermediate scattering function for a condensed phase of magnetic skyrmions. Skyrmions are magnetic quasiparticles with a helical magnetic structure. The direction of this helicity is a topologically protected quantity and gives the skyrmions a relatively long lifespan for such a complex magnetic object [23]. The system we chose to measure was a FeGd multilayer. At low magnetic fields this system has a striped magnetic phase. As the magnetic field is increased, the stripes break up into individual magnetic skyrmions. These skyrmions then orient into a hexagonal lattice. Using resonant magnetic x-ray scattering we can probe the magnetic structure of this lattice. These results show a scattering pattern with six fold symmetry [24]. By using two-pulse XPCS to measure the contrast as the skyrmion lattice peaks, we can obtain important information about the equilibrium fluctuations of the skyrmion lattice. This chapter will present the theoretical basis of the two-pulse XPCS method and the theoretical science of the FeGd multilayer.

3.2. Two-pulse contrast

In conventional XPCS, a series of speckle patterns is collected as a function of time. From this series, an intensity autocorrelation function, $g_2(\boldsymbol{Q}, \tau)$, is calculated and, using the theory from the previous chapter, the dynamic structure factor, $S(\boldsymbol{Q}, \omega)$, is obtained [25]. For our experiments on magnetic skyrmions, this structure factor contains crucial information about the magnetic fluctuations of a system and can be used to calculate the dynamic magnetic susceptibility. From theoretical work using the Landau-Lifshitz-Gilbert equation, we expect spin dynamics to occur in the nanosecond time scale [26]. Due to the sequential nature of the speckle patterns measured using conventional XPCS, the fastest accessible time scale is governed by the readout time of the detector [27].

To reach the faster time scales required to measure the dynamics of magnetic skyrmions, we instead chose to obtain the dynamic structure factor via two-pulse XPCS. In this method, the detector measures the sum of the scattering from two separate pulses delayed by tau for a series of thousands of events. Each pixel is measured individually as

$$S(\tau) = I(t_i) + I(t_i + \tau) \tag{3.1}$$

where $I(t_i)$ is the speckle pattern at particular time. The contrast of this speckle pattern is $C = \sqrt{\sigma^2(S)/S^2}$ where $\sigma^2(S)$ is the variance of the series of speckle intensities [28]. This contrast varies from 1, when the speckle patterns are identical, to 0.707, when they are uncorrelated. As the delay time is varied through the correlation time of the system, the speckle pattern will decorrelate allowing us to measure the time dynamics of the system.

We must now connect this contrast C to the summed intensity pattern [27]. The contrast also depends on $\boldsymbol{Q}$ but that will be suppressed for clarity. The normalized contrast is given by

$$C(\tau) = \frac{\langle S^2(\tau)\rangle - \langle S(\tau)\rangle^2}{\langle S(\tau)\rangle^2} \tag{3.2}$$

where the $S(\tau)$ expectation values can be expressed as follows:

$$\langle S^2(\tau)\rangle = \langle [I(t) + I(t+\tau)][I(t) + I(t+\tau)\rangle = 2\langle I^2\rangle + 2\langle I(t)I(t+\tau)\rangle$$

$$\langle S(\tau)\rangle^2 = \langle I(t) + I(t+\tau)\rangle^2 = 4\langle I\rangle^2 \tag{3.3}$$

Substituting into the contrast expression (3.2) we obtain

$$C(\tau) = \frac{2\langle I^2\rangle + 2\langle I(t)I(t+\tau)\rangle - 4\langle I\rangle^2}{4\langle I\rangle^2} = \frac{\sigma^2(I)}{2\langle I\rangle^2} + \frac{\langle I(t)I(t+\tau)\rangle}{2\langle I\rangle^2} - \frac{1}{2} \tag{3.4}$$

For a completely coherent beam $\frac{\sigma^2(I)}{\langle I\rangle^2} = 1$. We can use the Siegert relation from the previous chapter to rewrite the second term using the intermediate scattering function

$$C(\tau) = \frac{1}{2} + \frac{1 + |f(\tau)|^2}{2} - \frac{1}{2} = \frac{1}{2}(1 + |f(\tau)|^2) \tag{3.5}$$

giving us an expression for the contrast in terms of the intermediate scattering function. The above expression assumes a fully coherent beam. Incorporating partial coherence (β) gives

$$C(\tau) = \frac{\beta}{2}(1 + |f(\tau)|^2) \tag{3.6}$$

This shows that we can recover the same information as conventional XPCS using the two pulse technique by measuring the speckle contrast.

3.3. Speckle statistics

To measure the speckle contrast we must first understand the statistical properties of speckle. This is because shot noise and variations in the relative intensity of each pulse will cause the contrast to vary considerably between events. To obtain a reliable, unbiased estimator for the contrast we must collect a large number of events, on the order of ten thousand, and then analyze their statistical properties to determine the contrast. In addition, the measurement must be performed in the photon counting regime [29]. By remaining in the photon counting regime our CCD detectors can be used as high-resolution position sensitive photon detectors [30]. Using the classical optical theory of speckle [31], the probability distribution for observing k photons in a speckle is given by

$$P(k) = \frac{\Gamma(k+M)}{k!\,\Gamma(M)}\left(\frac{\bar{k}}{\bar{k}+M}\right)^{k}\left(\frac{M}{\bar{k}+M}\right)^{M} \tag{3.7}$$

where $\Gamma(x)$ is the gamma function, M is the number of modes in the speckle pattern and $\bar{k}$ is the average number of photons. The number of modes reflects the underlying dynamics of the system and is related to the contrast by $C = 1/\sqrt{M}$ [32]. If the system has dynamics slower than the delay time, then the speckle patterns will be completely correlated and the number of modes will be one. As the dynamics become faster than the delay time, the number of modes will increase and we can use the change in probability distribution to measure the dynamics of the system [27].

Using this theoretical framework, we can analyze the scattering and extract the dynamics of the system [33]. The first step is to collect a static scattering pattern. Using this we can select a region of interest that contains the scattering vector for the dynamics we want to study. Then the scattering intensity can be optimized to achieve good statistics. Finally, at each delay time of interest a series of two pulse events will be measured. These results with produce tens of thousands of raw detector images. This raw data must be converted into a photon map. Then, using this photon map, the speckle statistics can be calculated for each region of interest. Finally, they are fit, using nonlinear least squares, to the negative binomial distribution from equation 3.7. This will give a contrast value for each delay time and measurement condition. These values can be combined to obtain $S(\boldsymbol{Q}, t)$.

This relatively straightforward picture is complicated by several experimental concerns. First, the underlying theory assumes the speckle size is the same as the pixel size. The mean speckle size is given by [34]:

$$d_{speckle} = \lambda z / L \tag{3.8}$$

where z is the sample to detector distance and L is the beam diameter. This means that careful consideration must be placed on the location of the detector and its distance from the sample. Furthermore, because CCD detectors have some charge sharing between adjacent pixels, it is advantageous to actually have 4 pixels per speckle to allow reconstruction algorithms to better localize each photon [35, 36]. Second, this charge sharing by detector pixels means that the raw data must be refined using a droplet algorithm to determine the photons exact positions [37]. Otherwise a pattern with adjacent speckles would be counted as a single speckle with larger fluctuations which would artificially raise the measured contrast. Third, care must be taken to ensure the incident x-ray flux does not induce its own fluctuations or excitations in the sample or cause beam damage to the sample. Fourth, for each k there will be a slightly different distribution that can give a different measured speckle contrast. Therefore, each fitted contrast was combined in a weighted average. Fifth, the incident intensity must be carefully selected. It must be low enough to ensure that the scattering remains weak enough that theoretical speckle distribution is not disturbed by multiple scattering. It should also be low enough that individual speckles may be separately resolved. However, there must still be enough intensity that a sufficient population of higher k speckles are measured to allow for robust fitting. Finally, care must be taken to ensure that each pair of x-ray pulses has a similar flux and energy bandwidth. If the pulses differ too much then this will cause the speckle pattern to fluctuate and will artificially raise the measured contrast for the sample.

All of the above mentioned complexities can be managed and overcome with proper experimental design. First, careful consideration must be placed on the design of the x-ray source. The experiments were performed at the SXR beamline of LCLS. We chose to utilize the new two-bunch mode at LCLS [38]. This mode produces two separate pulses by using two different Ti:Sapphire lasers to create the x-ray pulses. Each pulse occupies separate radio frequency buckets giving delay times that are integer multiples of 0.35 ns up to approximately 50 ns. Because of radio frequency interference between some bucket configurations, many multiples are not allowed and some are more time consuming to configure than others. However, this still allowed us to scan over a reasonable range of delay times and demonstrate the viability of the technique. Second, a custom end station was designed that enabled us to mount the detector on a motorized flange far enough from the sample to get our desired four pixels per speckle while still retaining some motion to measure at different regions of the Q. Finally, we chose to measure the equilibrium dynamics of magnetic skyrmions in FeGd multilayer. This system has a novel skyrmion lattice phase that has been recently observed by our collaborators in the Eric Fullerton group and is predicted to have dynamics in the nanosecond regime [39].

3.4. Skyrmions

While originally a theoretical construct proposed by Skyrme in 1962 for nucleons, recent experimental results using small angle neutron scattering and Lorentz TEM have observed a variety of chiral magnetic skyrmions in thin film systems including MnSi [40], CoFeB [41], and FeGd [42]. Magnetic skyrmions are a localized quasiparticle of magnetic order. They consist of a vortex configuration of magnetic moments that form a topologically protected state [43]. This novel magnetic structure originates from competing magnetic interactions and admits a soliton solution that consists of hundreds of magnetic moments oriented in a vortex. This effect has been shown in a variety of magnetic systems where the competition between the exchange interaction and the Dzyaloshinskii-Moriya interaction stabilizes the formation of a chiral magnetic vortex as the lowest energy ground state. However, skyrmions have also been observed in transition metal – rare earth alloys where competition between long range dipolar moments, domain wall energy, and perpendicular magnetic anisotropy allow a skyrmion phase as the ground state configuration [44]. In these systems, a magnetic multilayer is created between two elements, Iron and Gadolinium in our case. These elements are antiferromagnetically coupled producing a ferrimagnet. By tuning the thickness of each layer and the strength of the magnetic moments the film can be engineered to have perpendicular magnetic anisotropy [45]. In these systems, a variety of magnetic phases can occur as a function of different temperatures and applied magnetic fields. One of the phases creates a chiral magnetic vortex in the Gadolinium spins. These dipole stabilized skyrmion occupy the entire thickness of the film, in our case approximately 80 nm, with a diameter of approximately 70 nm. Because the skyrmion is topologically protected state of the system, it is relatively stable and has been observed moving through films and forming long lived lattice-like ordered structures [46].

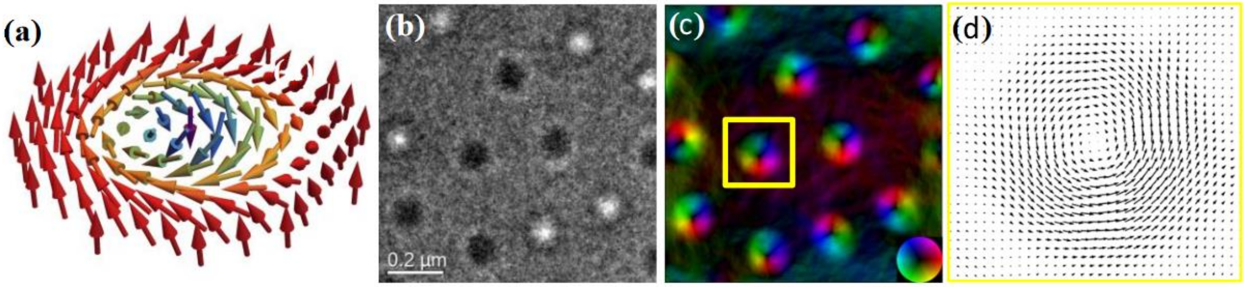

Figure 3.1: (a) Diagram of the spin structure of Bloch type skyrmion. (b) Underfocus Lorentz TEM showing skyrmions of both helicities. (c) Color representation of the in-plane magnetic induction calculated TIE analysis, hue and saturation indicate the direction and magnitude of the magnetic induction. (d) Vector representation of the in-plane magnetic induction [42].

For our work we chose a FeGd multilayer grown by the Fullerton group. This system consists of 100 repetitions of alternating Fe (0.34 nm) and Gd (0.4 nm) layers grown via DC magnetron sputtering and deposited on Si_3N_4 membrane [39]. This system was chosen because it has excellent tunability. Depending on the applied magnetic field, the system can be in one of three phases, hexagonal skyrmion lattice, disordered stripe phase, or ordered stripe phase. Furthermore, the samples overall thickness was optimized to maximize the scattered signal relative to its self-absorption. Before the XPCS measurements, the samples magnetic properties, including the hexagonal skyrmion lattice were characterized at the 12.0.2 soft x-ray beamline at ALS [47]. The measurements were performed in transmission geometry using forward scattering geometry.

3.5. Skyrmion lattice structure

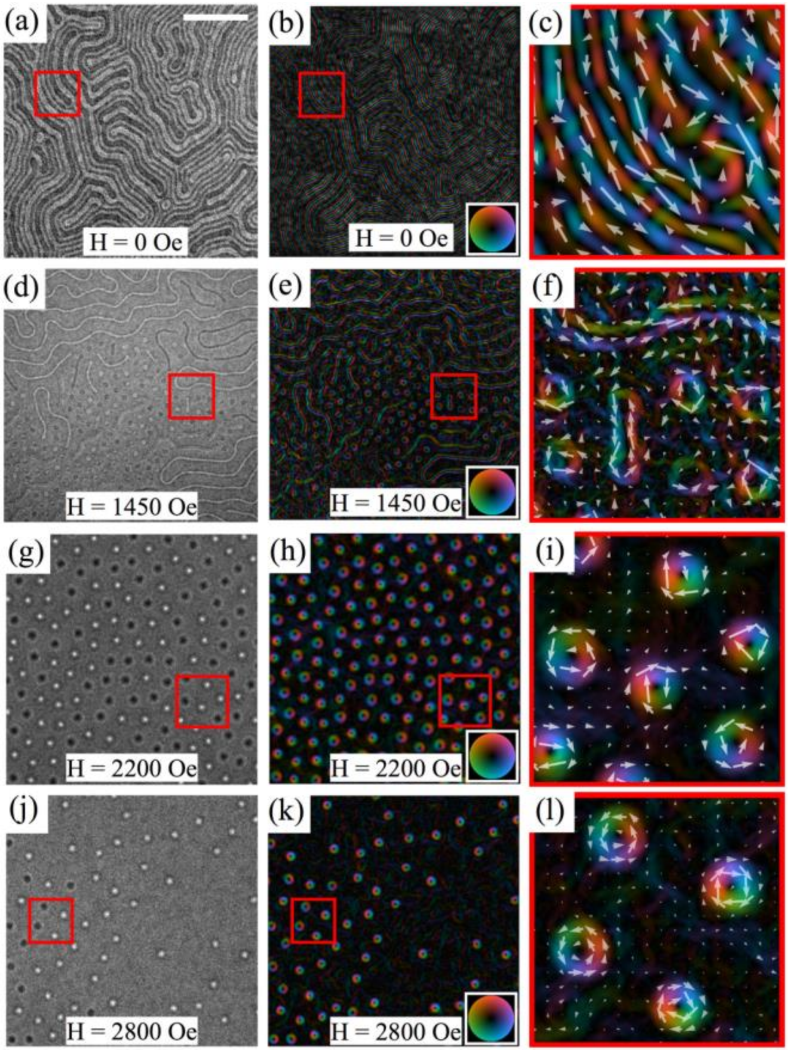

Figure 3.2: Real space Lorentz TEM imaging of field-dependent magnetic domain morphology in FeGd measured at room temperature. The first column is underfocused LTEM. The second column shows the magnetic induction color maps. The third column is a zoomed perspective of the second column with arrows indicating the in plane magnetization direction. Each row corresponds to a different magnetic phase: (a-c) disordered strip phase, (d-f) stripe-to-skyrmion transition phase, (d-f) hexagonal skyrmion lattice phase, (j-l) disordered skyrmion phase [39].

While isolated skyrmion phases do exist in FeGd multilayers at large applied fields, we chose to perform our measurement in the skyrmion lattice phase and ordered stripe phase. Each of these phase's real space magnetization was measured with Lorentz TEM and are shown in Figure 3.2. At zero applied field, the sample has a disordered stripe phase, known as labyrinth phase, with randomly oriented in-plane magnetic domains and strong Bloch domain walls. As the applied perpendicular magnetic field is increased, the stripes orient along the field direction [48]. This is referred to as the stripe phase. As the magnetic field continues to increase, the stripes parallel to the field grow while the stripes opposite to the field shrink. As they shrink they begin to collapse into cylindrical domains. Because the domains walls have Neel caps at their interface, these cylindrical domains can wrap around to form a three-dimensional magnetic vortex. This newly formed skyrmion will have a helicity $\gamma = \pm\pi/2$ depending on whether its cylindrical magnetization was clockwise or counter-clockwise. It is this helicity that is the topologically protected quantity that gives skyrmions their stability. Because skyrmions initially form from the stripe phase there will be a transition as more individual stripes are converted into rows of skyrmions. As these skyrmions form, they will move in the film into their lowest energy configuration, a hexagonal lattice [49]. During this transition, there will be coexistence between the two phases with some regions having a hexagonal skyrmion lattice while others are still in the stripe phase. As the magnetic field is further increased the remaining stripes switch to skyrmions. Eventually, the magnetic field becomes large enough that the skyrmions no longer sit in their lowest energy configuration. The hexagonal lattice breaks up into disordered isolated skyrmions.

While all of our measurements were conducted at room temperature, the full phase diagram of FeGd shows a rich pattern of states with multiple phases and transitions which can be explored in future work [50]. Each of the primary phases: disordered stripes, ordered stripes, and hexagonal skyrmions, has a distinctive scattering pattern. Because these are complex systems, the actual samples frequently contain defects that limit their order to relatively short length scales with little long-range ordering (see Figure 3.2). This causes the hexagonal lattice to only display first order scattering peaks. The ordered stripe phase domains mostly line up with the applied magnetic field but they frequently show kinks and other aberrations that also limit their long-range order. Consequently, both of the phases we measured display only short-range order. To calculate the static scattering pattern that each phase will produce, we take the Fourier transform of the real space lattice. To first order, the stripe phase produces two peaks aligned along the applied in-plane component of the magnetic field direction and the hexagonal skyrmion phase produces six hexagonal points in reciprocal space whose spacing are inversely proportional to the real space lattice constant. In the stripe phase, weak second order peaks are visible but their intensity proved too low to perform XPCS. The hexagonal skyrmion phase showed no higher order peaks. Furthermore, the messy ordering of both phases produces peaks that show considerable smearing from the theoretical delta function patterns one would expect from perfectly ordered states. However, for two-pulse XPCS, that contains a hidden advantage. Because the lattice peaks are spread over a larger area of detector, there are many more speckles to collect statistics and reduce the required measurement time.

The hexagonal skyrmion phase is of great technological interest as it provides a room temperature stable system to test the equilibrium fluctuations of magnetic skyrmions [51]. By tuning the x-ray energy to the Gd M_5 resonance, 1192 eV, we could measure the dynamic susceptibility of the skyrmion lattice. This will provide useful insight in the basic properties of a highly complex topological phenomenon and further the development of skyrmion based technologies. While skyrmions have existed as a theoretical concept for over fifty years, it is only recently, with the observation of magnetic skyrmions via neutron scattering [52], that practical application has become possible. Because a skyrmion’s helicity is a topologically protected quantity, it gives them a remarkably long lifespan for such a complex magnetic object

[53]. Their magnetic structure also means that they can be controlled by a spin polarized current in electronic devices [54]. The opposite helicities of the skyrmion also make them a promising candidate for information storage [55]. Skyrmions take very little energy to create relative to conventional flash memory. In addition, by tuning the growth conditions of the multilayer, the size of the skyrmions can be controlled. This enables smaller skyrmions to be used while increasing the information density of potential next generation memory. Finally, magnetic skyrmions can be a useful system for understanding the more general magnetic interactions in thin film systems. Skyrmions only form by balancing multiple competing magnetic interactions. Using two-pulse XPCS to understand the dynamics of this complex magnetic system will improve our understanding of magnetism more generally.

3.6. Conclusion

Two-pulse XPCS extends the time scale measurable by conventional XPCS by decoupling the technique from the speed of the detector. By moving the timing portion of the measurement from the detector to the x-ray source, a large regime of ultrafast dynamics can now be measured. Furthermore, some of the next generation of x-ray free electron lasers have the capability of producing pairs of pulse separated by even smaller delays than the nanosecond delays we used. These developments could potentially push two-pulse XPCS time resolution down into picosecond or even femtosecond regime.

Magnetic skyrmions provide a fascinating test case for our novel two-pulse XPCS technique. In addition to their possible applications in next generation magnetic memory technology, their complex magnetic ordering allows us to answer fundamental questions about magnetism. FeGd multilayers also display a number of different phases of skyrmions which allow us to measure the dynamics of the system in multiple configurations. Thanks to the tunability of FeGd multilayers, we were able to measure both the hexagonal skyrmion phase and the ordered stripe phase at room temperature by simply varying the applied magnetic field. This greatly simplified the experimental design and allowed us to bypass many technical problems that would ordinarily prevent such a novel measurement from being performed.

Chapter 4. Experimental results on skyrmion dynamics

4.1. Introduction

The experimental measurements using two-pulse XPCS on FeGd were taken over two separate runs. The first measurements were performed with modest goals and primarily designed to prove the viability of the technique. Only a limited number of delay times were tested and special attention was spent on testing and validating the supporting aspects of the measurement. The second measurements incorporated the knowledge we gained during the first experiment and the increased capabilities of the LCLS to expand the range of delay times we were able to measure. This allowed us to broaden our understanding of the skyrmion's behavior. In the first section, we will discuss some of the commonalities between the two measurements and some of the technical difficulties that we needed to overcome. Then, we will present the results from our first experiment. Finally, we present the results of our second experiment and summarize our findings.

4.2. Experimental considerations

Both of the measurements were performed at LCLS at the SXR beamline [56]. The photon energy was tuned to the M_5 edge of Gd, 1192 eV, using a 1001/mm monochromator [57], with bandwidth set by the exit slit to 1.0 eV [58]. A custom end station was engineered to mount the detector. For the first measurement, an Andor-Newton detector was placed 1.4 m from the sample. A spot size of 30 microns was achieved using a KB mirror system [59] resulting in a speckle size of approximately 13 microns. For the second measurement, a pnCCD detector was placed 2.4 m from the sample giving a speckle size of approximately 150 microns. Both detectors were run at 120 Hz to match the repetition rate of the LCLS. The detectors were mounted to the end station on a motorized flange that allowed the detectors to be moved around the scattering pattern to select the particular region to record data.

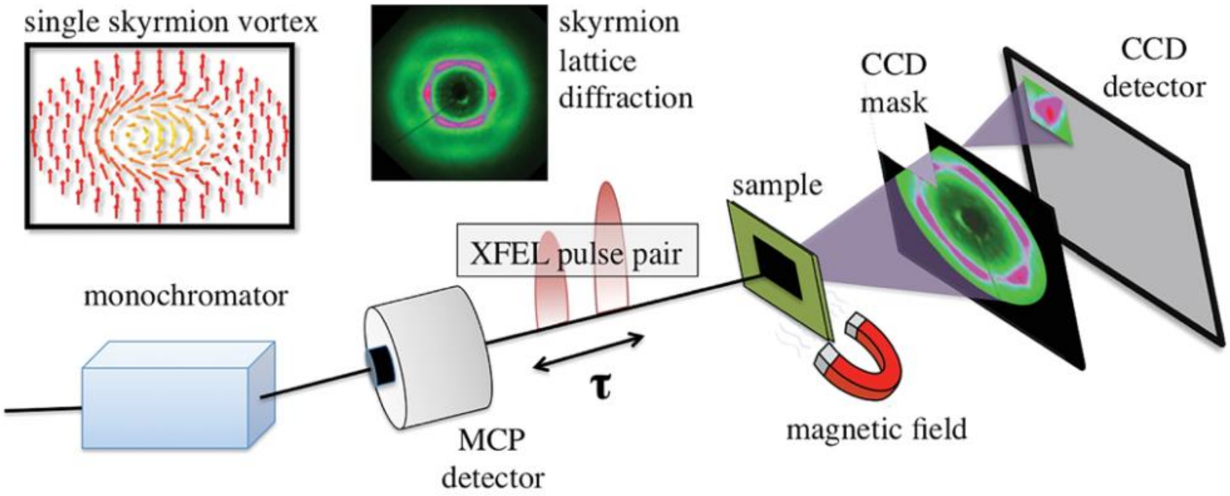

Figure 4.1: Schematic diagram of the skyrmion experiment. The MCP detector is used to measure the incident pulse intensity. The sample is placed in a magnetic field and illuminated with a pair of x-ray pulses. The scattering pattern from the skyrmion lattice is then collected on the CCD detector.

The two biggest technical challenges were processing the raw detector data into photon maps and monitoring the pulse intensities to ensure the intensity of each pulse remains equal. The two-pulse method depends on the statistical properties of the speckle pattern in the photon counting regime. Most of the speckles collected in the scattering pattern had only one, two, or three photons. This ensured that the detector stayed in the photon counting regime and the underlying assumptions used in the theory were maintained. This means that careful attention had to be paid to identifying the exact location of each photon. Second, our theoretical treatment assumed that two pulses of equal intensity would illuminate the sample and any changes in the speckle pattern are caused by the dynamics of the sample.

Unfortunately, the mechanics of two pulse generation regularly violate the above assumption. Therefore, we installed a multi-channel plate (MCP) detector on a SiN membrane into the beam flight path. The MCP has subnanosecond resolution and allowed us to characterize each pulse individually to ensure they had roughly equivalent intensity. First, single pulse data was collected to characterize the impulse response of the MCP. Due to an impedance mismatch with the amplifier, every single x-ray pulse produced a complicated ringing pattern in the MCP. This made it difficult to identify the intensity of the second x-ray pulse because the ringing from the first pulse could overlap with the second pulse. We developed a numerical process that computed the pseudoinverse of the two-pulse signal, then multiplied this by two scaled reference signals from the single pulse results. This provided a numerically stable method of computing the intensity of each pulse. We initially tried to use non-linear least squares to fit two individual pulses to the combined signal. Unfortunately, some of the events only had one x-ray pulse and this caused the fitting algorithm to produce unreliable results. Because each measurement contained over one hundred thousand events, even a small fraction of incorrect fitting results could bias our final results. For pulses that differed in intensity by more than twenty percent, the data was discarded.

This MCP was used on the first day of measurements to determine the distributions of the pulse intensities. We found that the first pulse was on average fifty percent more intense than the second pulse. Each pulse is generated by a separate laser causing each pulse to have a different spectrum. Once, the pulse passes through the beamline monochromator they could have widely different intensities. This meant that the first day’s results only produced around one percent usable data where both pulses had equal intensity. We therefore had to build a real-time intensity monitor for the pulse intensity and then supply it to the linear accelerator staff at LCLS. Using this tool allowed them to tailor the pulse amplification process to balance the intensity between the pulses. This improved the ratio of usable events, where each pulse has equal intensity, to around ten percent. This process was refined during the time between the first and second experiment. The MCP's electrical properties were tuned to reduce impedance mismatch and a thorough characterization of its impulse response was performed to improve the robustness of the numerical fitting. This investigation demonstrated that some of the events actually contained only one pulse as the second laser bunch was mistimed relative to the accelerating currents. The LCLS accelerator group used these finding to optimize the two-bunch generation process. On the second experiment we achieved around twenty percent usable events.

For the first experiment, the detector used was an Andor-Newton. This is a CCD x-ray detector optimized for soft x-ray energies. It has a small pixel size of 16 microns by 16 microns arranged in array of 1600 by 400. Because of the small pixel size, the pixels were processed in blocks of four to reduce noise and more closely match the size of the speckles. This detector could be run in two separate modes. The first mode used the entire pixel array. This enabled it to capture the entire small angle scattering pattern. This mode can only be run at 2 Hz so it could only be used for static scattering analysis and alignment. The second mode only uses a small corner of the detector, 90 by 90 pixels, but can be run at the full 120 Hz. This mode was used to collect the speckle patterns used in the XPCS analysis. Because of the limited field of view, speckle could only be collected for a single peak from the scattering pattern at one time. For the hexagonal skyrmion phase, two different peaks were collected to ensure reliability of the measured speckle statistics.

For the second experiment we used a pnCCD detector. This detector has a much larger 75 micron by 75 micron pixel size which required it to be mounted further from the sample. The imaging array is 1024 by 1024 pixels and the detector can be run at the full 120 Hz using the entire area. This means that the entire scattering pattern could be collected and we could compare the speckle contrast for each of the six hexagonal skyrmion peaks. In addition, by having the entire scattering pattern for every run we could compare the static scattering features to monitor for any structural changes.

While both detectors had different measurement properties, the data processing pipeline developed was relatively similar [30]. First, the dark current background was subtracted. Then, the common mode noise filter was applied. Next, the differential pixel sensitivity was corrected for. Then, a thresholding filter was applied to identify all pixels that had counts above the background. These pixels were then clustered into groups of adjacent pixels. All adjacent pixels that had counts above the threshold were combined using an image segmentation algorithm. This created a list of individual speckles in the image. After this process, we had a map of corrected intensity counts separated into individual speckles that needed to be converted into photon positions. When a soft x-ray photon strikes the detector, its charge is shared by the adjacent pixels. This means that each individual photon produces a small blob of counts across several neighboring pixels where the total integrated counts sum to the energy of the photon. These blobs are referred to as droplets. To convert these blobs of detector counts into a map of photons in each speckle, a droplet algorithm was used [60]. This process involves modeling every photon as a two-dimensional Gaussian intensity pattern. Then allocating Gaussians proportional to the integrated counts of each droplet and using nonlinear least squares to numerically fit the photon positions [61]. This algorithm is very computationally expensive and prevented real time data analysis during the experiment. Once the photon map was calculated, the regions of interest were created around the different scattering peaks. The mean photon probability and photon population statistics were then fit, using nonlinear least squares, to the negative binomial distribution (equation 3.7) to obtain the number of modes. This fitting was repeated for each k, number of photons, and then a weighted average was constructed to finally determine the speckle contrast. This process was repeated for each delay time and magnetic field.

4.3. First set of experimental results

For our first measurement, we had modest goals of measuring a few delay times for the hexagonal skyrmion phase and the stripe phase. There was a limited range of delay times the accelerator could produce: 0.7 ns, 4.55 ns, 8.75 ns, and 26.25 ns. These delay times, together with zero delay, allowed us to make a preliminary sketch of the correlation function. The primary objective was to determine the viability of the two-pulse technique. This involved characterizing the intensity distribution of the pulses, verifying that the sample chamber and detector could collect the skyrmion scattering pattern, and understanding the statistical properties of speckle to see how they compared with theory.

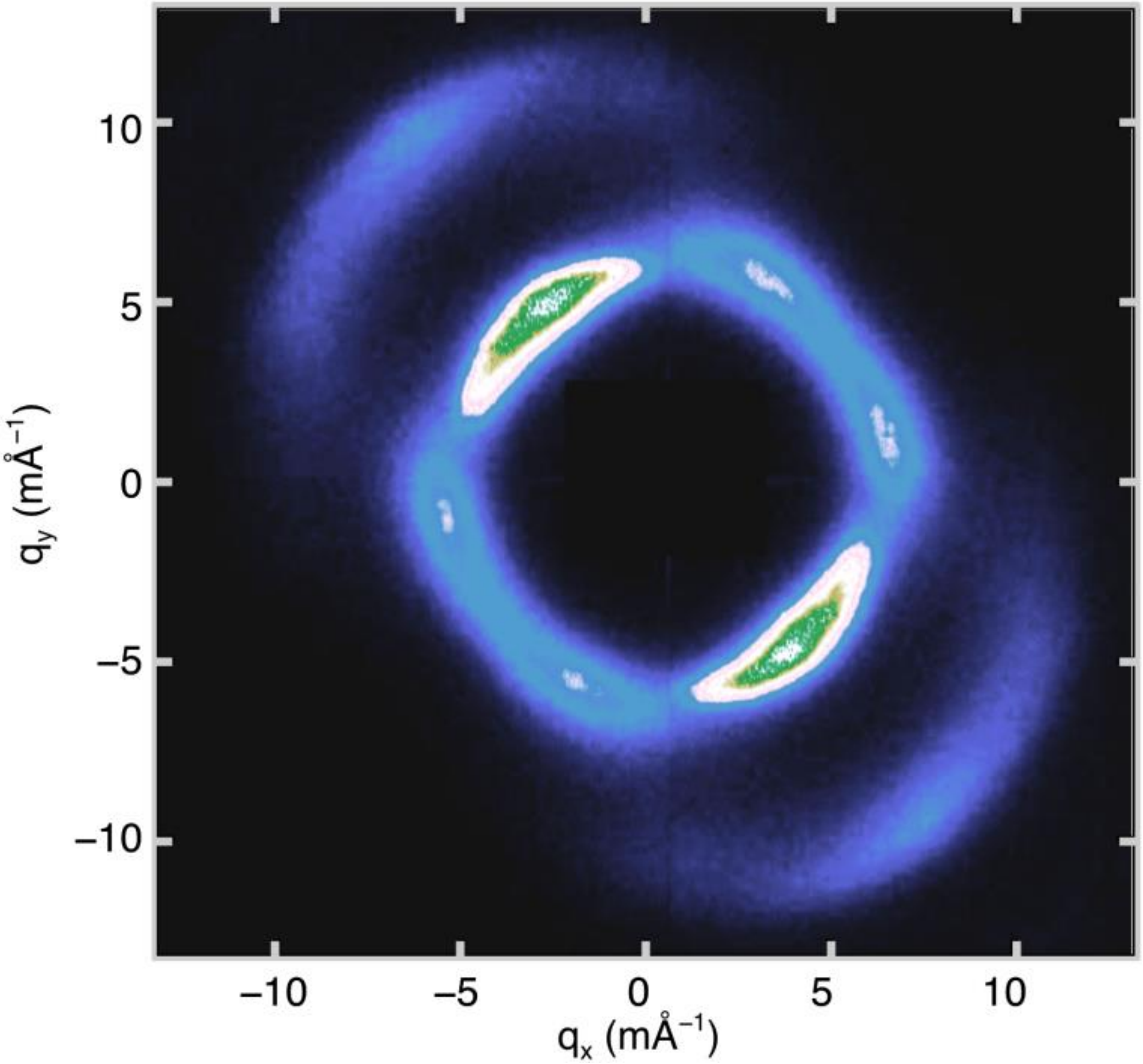

Figure 4.2: Average scattering pattern in the stripe-to-skyrmion transitional phase.

The first stage of the measurements consisted of sweeping the applied magnetic field to determine the onset of the skyrmion phase transition. To create the skyrmion phase in the FeGd multilayer an out-of-plane magnetic field must be applied to the film. A small in-plane magnetic field assists the formation of the skyrmion lattice [48]. To achieve this, an out-of-plane electromagnet was mounted with a tilt of 3.5°. This allowed us to create the magnetic field conditions required to form the skyrmion lattice. The measurement was performed by collecting the entire scattering pattern using the low speed detector mode and monitoring the scattering around the maximum of the six-fold peaks characteristic of the skyrmion lattice phase (see Figure 4.2). This occurred at 210 mT and matched the applied magnetic field that was measured during characterization done at ALS [39].

Next, we performed several measurements at a variety of x-ray fluences to ensure the beam was not damaging the sample or producing excitations. This is important because the goal was to measure the equilibrium dynamics of the skyrmion lattice. However, we did not know what these excitation energies would be, so a series of increasing intensity measurements were performed. Given the beamline optics and x-ray wavelength, we calculated the maximum dose for our measurements as $\approx 10^{-3}$ eV/atom. The damage threshold for the sample was 0.4 eV/atom. When the fluence reached 0.04 eV/atom we started to see nonlinear effects showing the excitation threshold. We then took a series of XPCS measurements at multiple energies below this value and found the same measured contrast as a function of incident intensity.

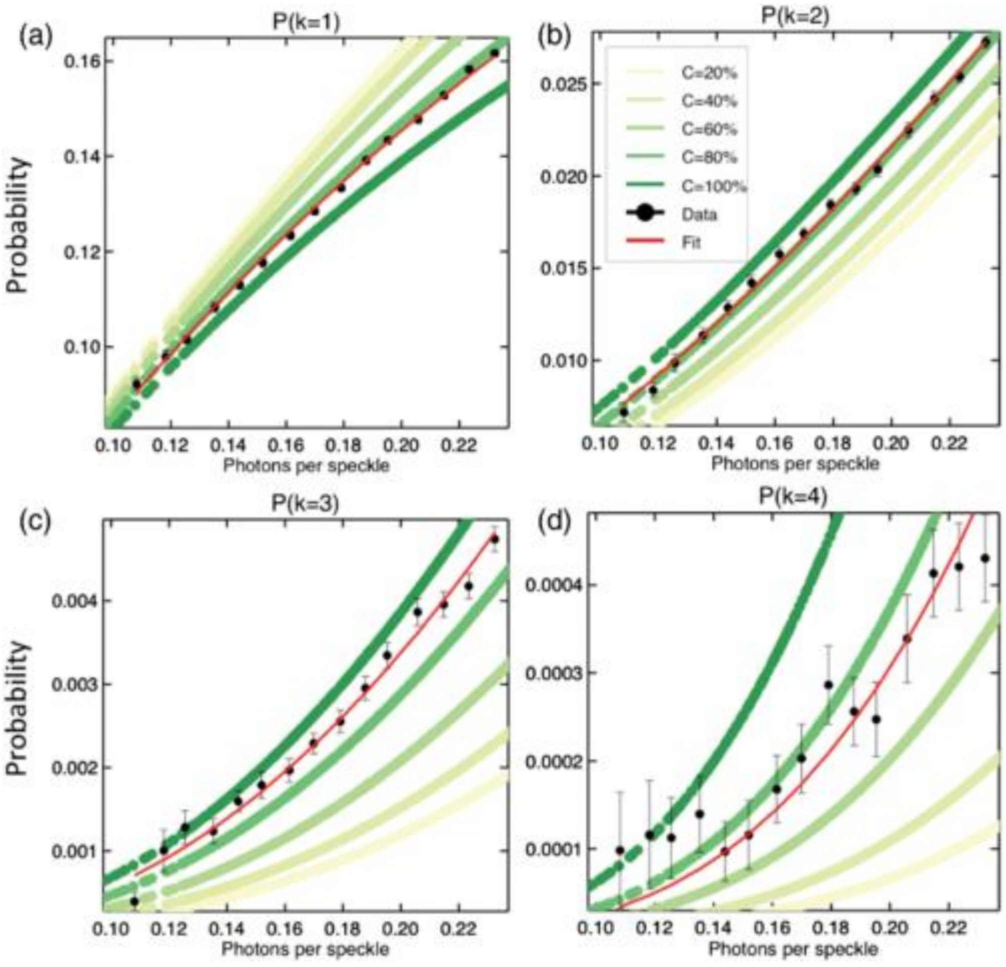

Figure 4.3: Probability of measuring k photons in the skyrmion peak for $k = 1 - 4$ in (a)-(d) respectively plotted against the average photon density $\overline{k}$. The black dots are the data and the red line is the best fit line. The green curves represent the potential probabilities from a range of contrasts.

Once the tuning and validation mentioned in the previous section was completed, we collected data for the stripe phase, the hexagonal skyrmion phase, and at an intermediate magnetic field that is a transitional field between the two phases. Modeling was then performed to simulate the different probability distributions we would expect to find for a variety of contrasts (see the green curves in Figure 2.1). These were then compared to verify that the results were consistent with the theory. Our initial results proved rather inconsistent. We then undertook a more careful study of the detector dynamics and made several enhancements to the droplet algorithm that improved the accuracy of the photon map generation process. With this new data processing pipeline, we were able to obtain more consistent results. The intensity of the x-ray scattering pattern limited us to only using $k = 1,2,3,4$ photon events as larger values of k did not have sufficient statistics. Each of these k values where then fit to the negative binomial distribution (Equation 3.7) to obtain the contrast (see Figure 4.3). We also fit the ratio $\alpha(k) = P(k)/P(k+1)$ for $k = 1$. This enforces self-consistency while also measuring the contrast.

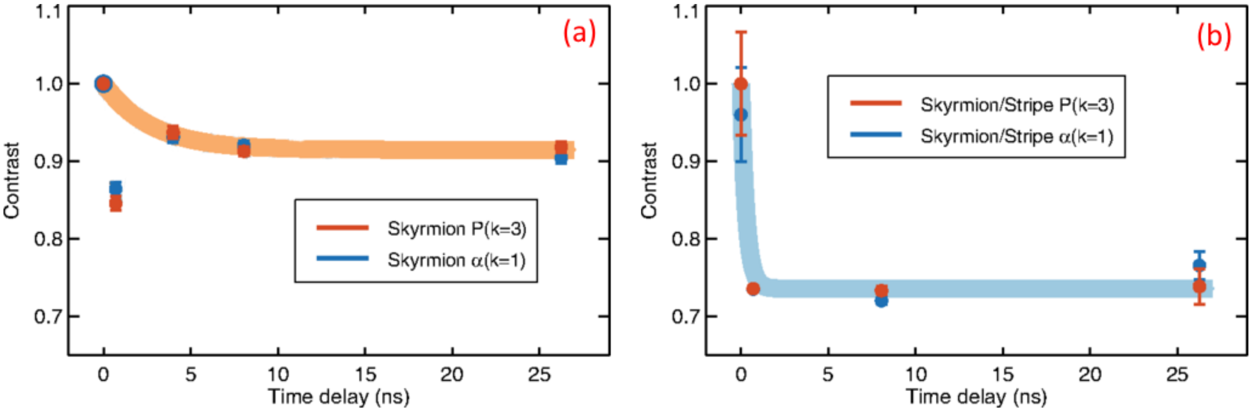

Figure 4.4: Contrast vs time for each magnetic phase. The blue points are calculated based on fitting α(1). The red points are the fitted contrast for P(k=3). (a) Results for the Skyrmion phase at 210 mT. The orange curve shows a fit using an exponential decay with a decay time of 4ns (b) Results for the skyrmion stripe transitional phase at 200 mT. The blue curves shows a fit using an exponential decay with a decay time of 300 ps.

For both magnetic phases, the probabilities we measured showed the contrast decaying as the delay time was increased. Using our limited data points available, we choose to fit a simple exponential decay to the weighted average. For the hexagonal skyrmion phase, we found a decay time of 4 ns (see the orange curve in Figure 4.4a). And while having only five data points limited the precision of the result, the data shows a gradual loss of contrast over the time scale measured. This is significantly different from the results measured while the sample was in the transition between the skyrmion phase and the stripe phase. In this data the decrease in overall contrast is much higher, near the maximum decorrelation value of 0.707, and the time constant for the decay is much faster, 300 ps (see Figure 4.4b). The results for the pure ordered stripe phase were even faster than the transition phase and proved to be faster than the lowest delay time we could measure.

While the number of data points obtained in our first experiment were limited, they did demonstrate the viability of the technique. Furthermore, our results were consistent with other skyrmion work including neutron spin echo [62] and ferromagnetic resonance [39]. These results also contributed to a more precise understanding of the Andor-Newton detector in the photon counting regime and a better operational understanding of the capabilities of the two-pulse mode of LCLS. We also created several real time data processing tools to allow preliminary analysis of the measurements. This proved invaluable during our second experiment where we were better able to focus our measurement time on the delay times and magnetic fields that proved most interesting.

4.4. Second set of experimental results

For the second experiment, three primary changes were made. First, a new pnCCD detector was used. This detector has larger pixels and a larger collection area which enables it to measure the entire scattering pattern at the full 120 Hz speed. It also had lower dark current and less charge sharing between pixels which simplified the data processing pipeline. Second, the electrical properties of the MCP were improved and a real time monitoring application was developed for the accelerator group that allowed around twenty percent of events to have two pulses with equal intensity. Finally, improvements to the LCLS facility had decreased the amount of time spent setting up each delay time. These improvements allowed for eleven different delay times (0.7, 1.05, 1.75, 2.1, 2.8, 3.85, 4.55, 5.25, 8.75, 15.75, 26.25 nanoseconds) to be measured which gave a more complete view of dynamics. All of these improvements meant that we collected roughly a thousand times more data in the same four shifts of measurement.

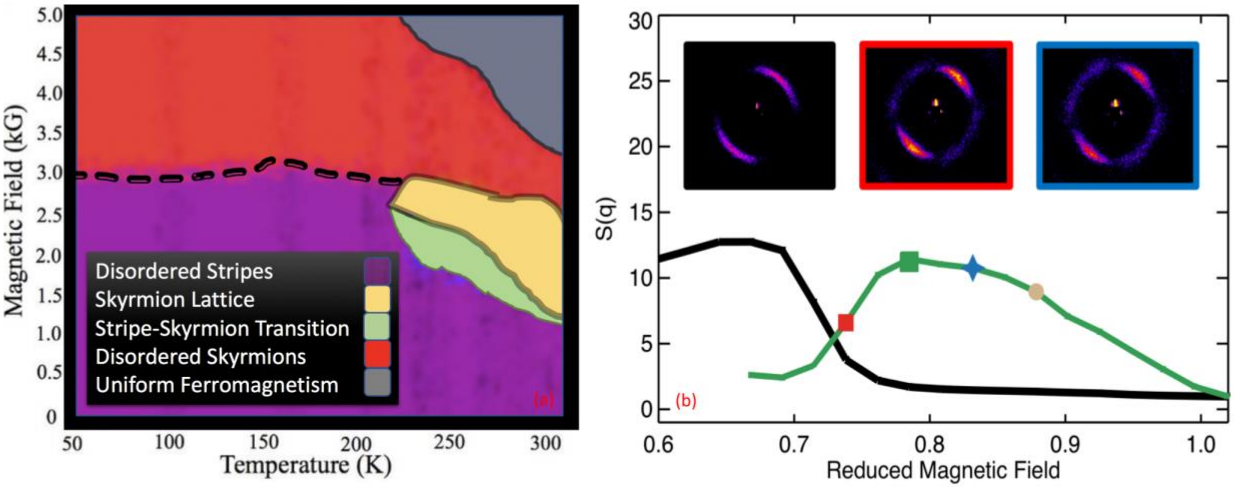

Figure 4.5: (a) Magnetic field and temperature phase diagram for the FeGd multilayer [39]. (b) The black curve is the total integrated scattering for the stripe phase peaks and the green curve is the total integrated scattering for the skyrmion phase peaks as function of magnetic field. The markers represent the magnetic fields where XPCS measurements were performed. Inset shows the scattering pattern for the stripe phase, the skyrmion phase, and the stripe skyrmion transition phase from left to right.

Using the full frame capabilities of the new detector, a full study of every scattering peak as a function of applied field was performed to map the phase diagram. This showed the full transition from the stripe phase, through the mixed phase, into the skyrmion phase with the characteristic hexagonal symmetry (see Figure 4.5b). During this transition we observed a subtle change in the scattering. As the magnetic field increased, the Q of the stripe peaks increased from $6.2 \times 10^{-3}\text{Å}^{-1}$to $6.3 \times 10^{-3}\text{Å}^{-1}$. This slight increase in Q coincided with the emergence of the hexagonal skyrmion peaks. In addition, the width of the stripe peaks also increased with increasing magnetic field. These results indicate the spacing between the stripes became smaller and more disordered as the multilayer transitions into the skyrmion phase. This supports the Lorentz TEM results that show the skyrmions forming as individual stripes are compressed and break into strings of skyrmions [39]. Due to these results, we chose several magnetic fields to perform our measurements. The scattering at each magnetic field is shown in Figure 4.5b. The first point, red square, is the transitional stripe-to-skyrmion phase and was measured at 195 mT. The second point, green square, is the maximum of the skyrmion scattering and was measured at 210 mT. The third, blue star, and fourth point, tan circle, points were chosen as the skyrmion scattering gradually declined to observe the dynamics of the skyrmion lattice as it decayed. They were measured at 220 mT and 235 mT respectively. The results in the following figures are color coded to match the magnetic field values from Figure 4.5b.

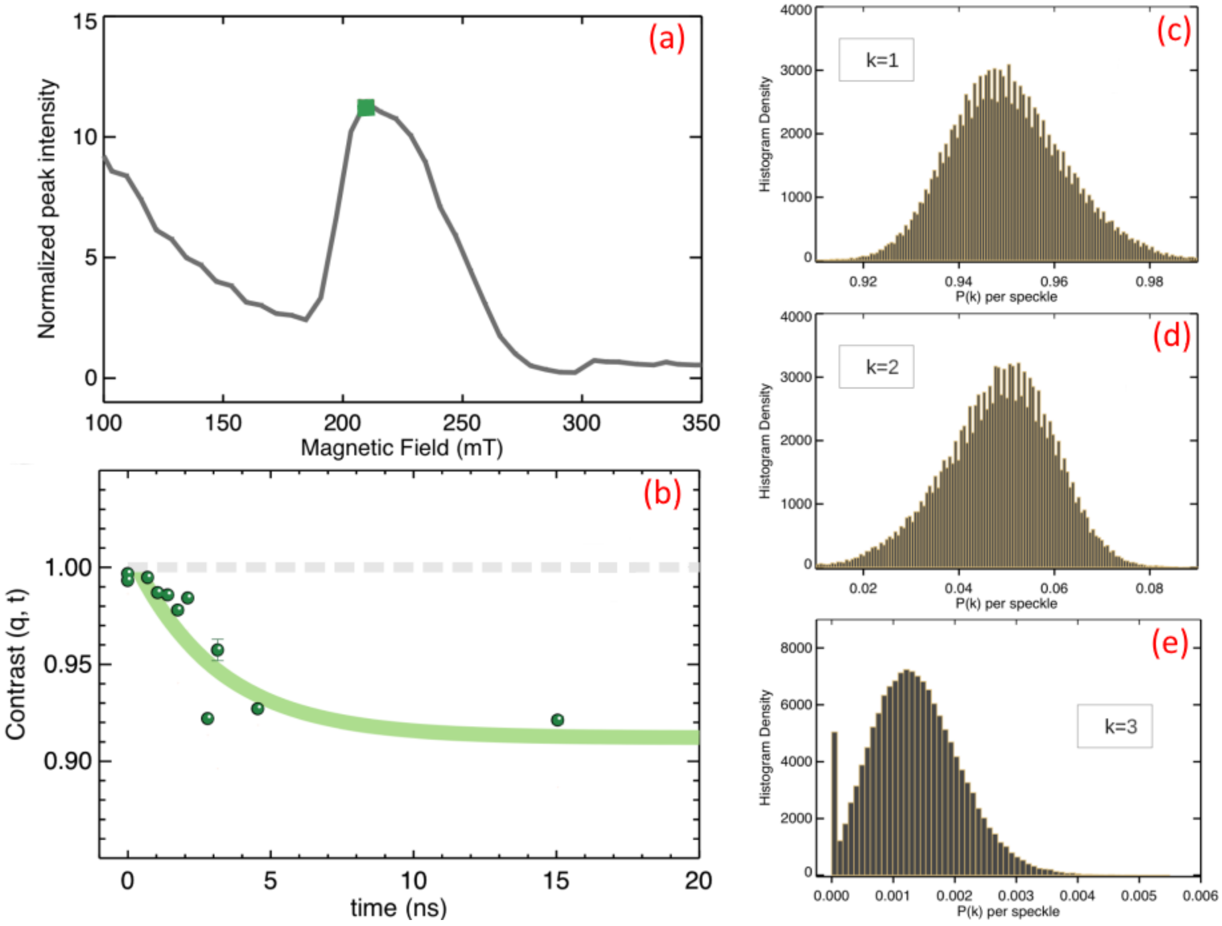

Figure 4.6: (a) The integrated intensity of the skyrmion lattice peak as function of magnetic field. The green square indicates the skyrmion phase magnetic field value, 210 mT. (b) The speckle contrast for the skyrmion lattice phase. The green curve is fitted with a compressed exponential decay with a time constant of 3 ns. (c-e) Histograms of the probability density of measuring k-photon events.

At the peak of the skyrmion phase, we measured a decaying exponential with a decay constant of 3 ns (see Figure 4.6b). This result is reasonably close to our first measurement but incorporates double the number of delay times. Each delay time also contains significantly more data than the previous experiment. Because we could collect the entire scattering pattern we were able to average all six skyrmion peaks. To determine the regions to use for each peak, the average Q of the hexagonal lattice was found to be $6.3 \times 10^{-3}\text{Å}^{-1}$. Then an average image was computed from all of the resonant scattering patterns after normalizing each image to the incident intensity measured by the MCP. To this image, a separate two-dimensional ellipse was fit to each of the six skyrmion peaks. The average photon intensity, $\bar{k}$, was computed for each peak and then the photon probability distributions were calculated (see Figure 4.6c-e). These distributions were fit to the negative binomial distribution and we obtained a similar contrast for each peak. Finally, a weighted average was computed for one, two, and three photon events to give the final contrast for each delay time.

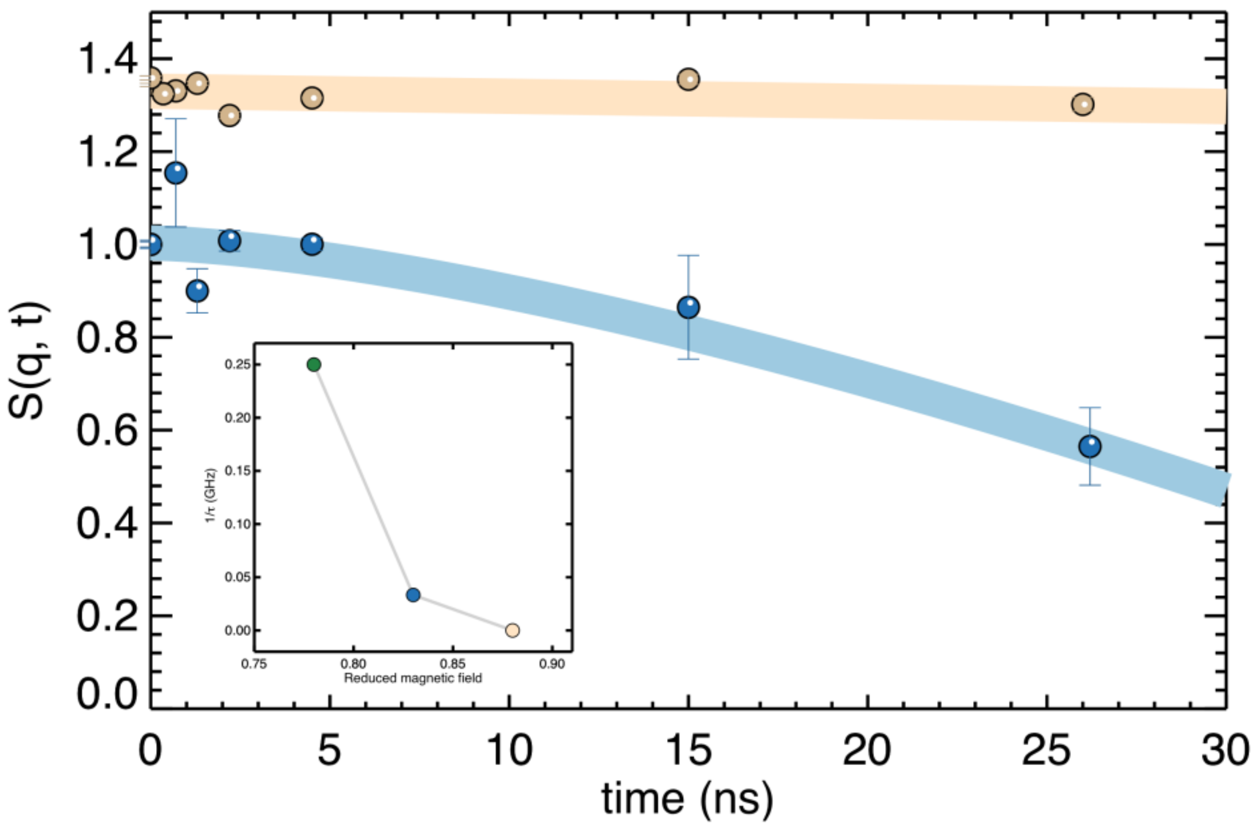

Figure 4.7: Speckle contrast for magnetic field 220 mT, blue, and 235 mT, tan. Both points are at a magnetic field where the skyrmion lattice phase is decaying. Each has been fit with a compressed exponential. The tan curve shows no dynamics. The blue curve has a decay time of 30 ns. The inset shows the timescale $1/\tau$ vs reduced magnetic field, this is the ratio of the magnetic field to the critical magnetic field where the skyrmion phase disappears. This suggests critical behavior as the skyrmion phase decays.

The third magnetic field point, 220 mT, and fourth magnetic field point, 235 mT, were chosen to capture the dynamics of the skyrmion lattice as it breaks down. These points are 82% and 88% of H_c, the magnetic field were the hexagonal skyrmion lattice decays into a disordered skyrmion state. The same procedure outlined in the previous paragraph was used to determine the contrast although due to instrumental concerns, a slightly different set of delay times were measured. The third point, in blue, shows a much slower decay time than the peak skyrmion phase. The fitted time constant is 30 ns. For the fourth point in tan, no decay is shown on the time scale we could measure giving a relatively static speckle contrast. While not definitive, these results showing an increased delay time with increased magnetic field point to critical behavior. As the skyrmion lattice decays the long-range order disappears as it breaks up into islands of short-range order. Our results show that these smaller clusters of skyrmions have much slower dynamics that are beyond the time resolution of our measurement capabilities.

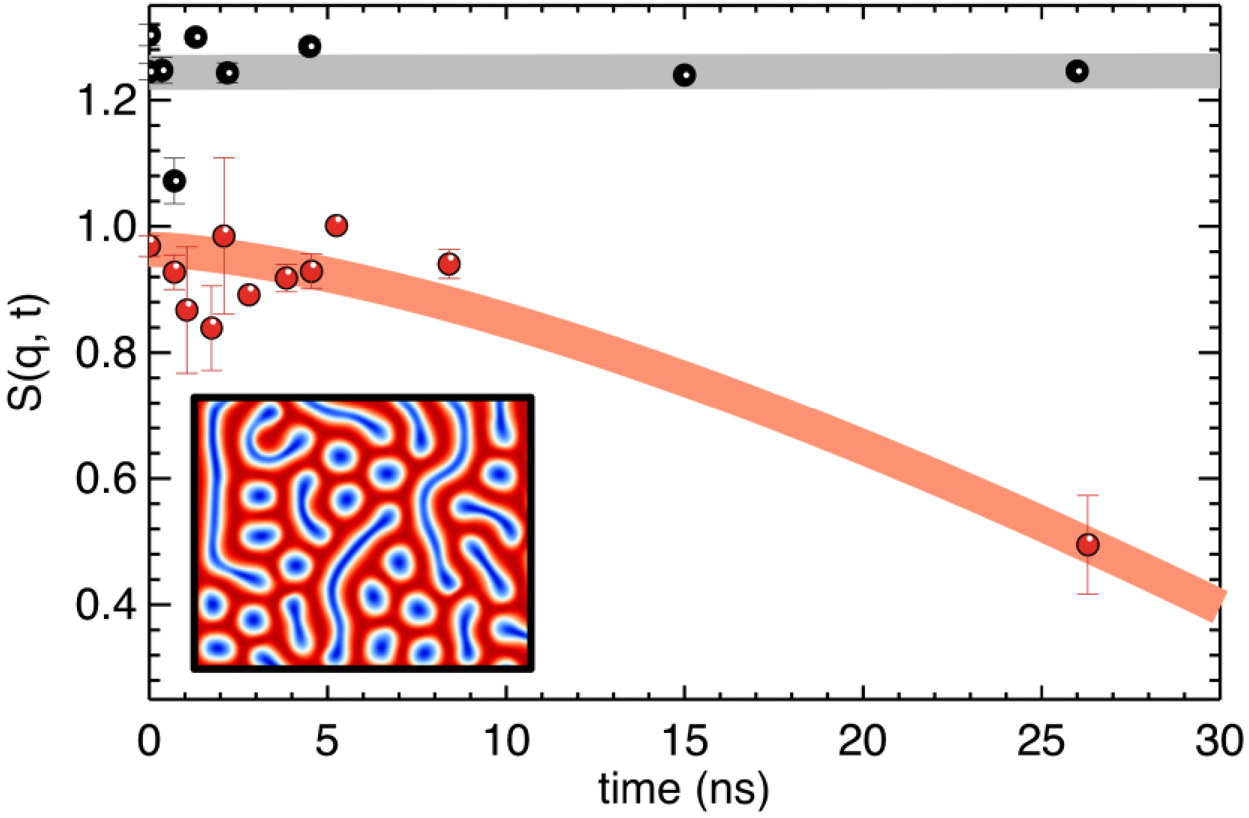

Figure 4.8: Speckle contrast for stripe-to-skyrmion transition phase. The red curve is fitted with a compressed exponential decay with a time constant of 30 ns. The grey curve is single pulse contrast and shows no change with time. The inset shows a simulation of the real space magnetization of the strip-to-skyrmion transition phase [39].

Measurements at 195 mT show the dynamics at the transition between stripe phase and skyrmion phase. Here the scattering pattern is instructive (see Figure 4.2). It shows two bright peaks along the diagonal characteristic of the stripe phase and four more peaks arranged circularly. The radial Q vector for the four skyrmion peaks is slightly larger than that of the two stripe peaks. Furthermore, the elongated shape of the stripe peaks suggests that the two missing skyrmion peaks are simply being overwhelmed by the much brighter stripe peaks. Given the impossibility of separating their dynamics from the brighter stripe peaks, we used only data from the four clear skyrmion peaks. Here, a simple exponential decay proved a poor fit to the data. Instead a compressed exponential, called a Kohlrausch-Williams-Watt function, was fit to

$$S(q,t) = A_0 \exp\left(-\frac{t}{\tau_0}\right)^{\beta} \tag{4.1}$$

with 30 ns delay time and a stretching exponent of $\beta = 1.7$. This stretching exponent is commonly seen in soft matter systems and other jammed systems [63, 64]. Jamming typically occurs in glassy systems as a manifestation of non-Gaussian dynamics between two distinct phases [65]. In our class, both the scattering pattern and the stretching exponent show a mixed phase between stripes and skyrmions as in undergoes a nuclear style phase transition. The regions of stripe phase limit the equilibrium motion of the skyrmion regions lead to jamming behavior.

4.5. Conclusion

Overall, these different magnetic field conditions paint a rough picture of the equilibrium fluctuation of the skyrmion lattice. At its maximum intensity, the dynamics are relatively fast, around 3 ns. Our results provide a direct measurement of the equilibrium fluctuations of the skyrmion lattice. This can be used to better understand the stability of skyrmions which will prove crucial to their application in future electronic devices. As the magnetic field is either increased or decreased, the dynamics begin to slow down. At the lower magnetic field, the transition from the stripe phase into the skyrmion phase shows jammed dynamics. While at higher magnetic fields, the dynamics slow until they exceed our measurement capabilities. At both of these magnetic fields, the measured speckle contrast shows a compressed exponential behavior. This is indicative of jammed dynamics and provides a valuable insight into the dynamics of the creation and destruction of the skyrmion lattice. These results also show critical behavior as the skyrmion lattice decays and breaks up into islands of disordered skyrmions.

Our results also demonstrate the viability of two-pulse XPCS. We successfully applied this novel technique to use coherent x-rays to measure dynamics on a time scale previously only accessible via neutron scattering. By combining two-pulse XPCS with resonant magnetic x-ray scattering, we were able to measure the magnetic dynamics of a complex system. This opens up a wide range of experiments where it is impossible to create a sample of sufficient size for neutron scattering. In addition, this extends the time scale available to x-ray scattering. Conventional XPCS is limited by the speed of x-ray detectors, currently around 0.1 milliseconds. But by using the two-pulse method, this limit is removed and coherent x-rays can be using to measure dynamics limited only by the spacing between x-ray pulses. Current work at LCLS on the hard x-ray split and delay beamline shows the potential to measure dynamics on the picosecond time scale. By demonstrating the viability of this technique, we have opened the door to a wide range of ultrafast measurements using two-pulse XPCS.

The text in Chapter 4 is based on material published in

M. H. Seaberg, B. Holladay, J. C. T. Lee, M. Sikorski, A. H. Reid, S. A. Montoya, G. L. Dakovski, J. D. Koralek, G. Coslovich, S. Moeller, W. F. Schlotter, R. Streubel, S. D. Kevan, P. Fischer, E. E. Fullerton, J. L. Turner, F.-J. Decker, S. K. Sinha, S. Roy, J. J. Turner, Nanosecond x-ray photon correlation spectroscopy on magnetic skyrmions. *Phys. Rev. Lett.* 119, 67403 (2017). The dissertation author was a major contributor to this paper.

The text in Chapter 4 is based on material that has been submitted for publication in M. H. Seaberg, B. Holladay, X. Y. Zheng, J. C. T. Lee, A. H. Reid, S. A. Montoya, J. D. Koralek, G. Coslovich, P. Walter, S. Zohar, V. Thampy, M. F. Lin, P. Hart, K. Nakahara, R. Steubel, S. D. Kevan, P. Fischer, W. Colocho, A. Lutman, F.-J. Decker, E. E. Fullerton, M. Dunne, S. Roy, S. K. Sinha, J. J. Turner. Magnetic Skyrmion Fluctuations. The dissertation author was a major contributor to this paper.

Chapter 5. Battery polymer electrolytes

5.1. Introduction

Batteries are one of the cornerstone technologies of modern life. They enable our portable electronic devices and are increasingly finding their way into cars and electricity distribution grids. Currently, batteries enable a huge range of portable electronic devices. These devices are integral to contemporary life. For many of these products, battery performance is the primary limitation on their overall performance, capability, and size. As the threat from climate change grows, society will need to meet our increasing energy demands with more variable renewable energy sources. Batteries will be a crucial technology to average out the fluctuations in energy demand and allow the world to transition to renewable energy future while maintaining our standard of living [66]. In addition, the rise of electric vehicles opens a huge new market for battery technology. For automotive applications, batteries must have both high performance and excellent stability to survive the rigors of vehicular environments [67]. These batteries will be deployed in a huge variety of environments to provide low emissions power and be expected to last far longer than the current generation of batteries used in portable electronics. This explosion of demand for batteries will continue to push research forward as battery performance takes a central role in the coming years. Much of the current research in battery technology is focused on engineering type questions that seek to improve energy density, longevity, or stability through iterative refinements of current technology [68]. Despite their widespread applications, many basic science questions about batteries remain. Questions about the mechanics of ion transport, the behavior of electrode electrolyte interfaces, and how dendrite growth affects long term stability are still unanswered [69–71]. In this chapter, we will provide experimental insight into the mechanism of ion transport in polymer battery electrolytes.

For portable electronics and other environments where weight is a primary concern, the dominant battery chemistry is Li-ion. These contain electrodes made of a graphite anode and lithium cobalt oxide or lithium iron phosphate for the cathode. The electrolyte is typically a liquid organic solvent such as ethylene carbonate or dimethyl carbonate. A salt of Li ions and a counterion are then dissolved into the electrolyte. These ions perform the electron transport that powers the battery. These electrolytes have high conductivity and offer good performance [72]. However, they are also flammable, toxic, and corrosive presenting a major safety concern [73]. This makes Li-ion batteries very sensitive to physical shocks because even small damage to a single cell can cause the electrolyte to spill and damage adjacent cells. This can lead to a cascading failure and can cause the complete destruction of the device [74]. Furthermore, if the battery short circuits due to improper charging or degradation over time the current spike will create a rapid rise in temperature [75]. This can cause a thermal runaway reaction in the damaged cell leading to its rupture. The hot flammable liquid electrolyte can then leak from the ruptured cell causing the damage to spread and rapidly leading to an uncontrollable fire [76]. Finally, a liquid electrolyte provides no structural stability and is susceptible to damage via shear forces [77].

To address these safety concerns, solid polymer electrolytes have been proposed as an alternative. They were first discovered by Wright in 1973 [78]. These polymer electrolytes are non-flammable and do not contain corrosive or toxic chemicals typically found in liquid electrolytes. They are far more resistant to high temperature and physical shocks than liquid electrolytes [79]. Furthermore, the increased rigidity of polymers can provide structural support to the battery and reduce weight by removing the need for heavy structural packaging [80]. Working with our collaborators in the Mike Toney group, we chose to use a model battery system of Lithium bis(trifluoromethane)sulfonimide (TFSI) as the salt and polyethylene oxide (PEO) as the polymer. PEO/LiTFSI is a well-studied system with a large amount of research exploring its properties [81–84]. In addition, it's a promising real-world candidate for future solid polymer electrolyte batteries [85]. TFSI is an excellent anion because it has one of the highest dissociation constants of the commonly used Li salts and good resistance to clumping [86, 87]. PEO is the primary polymer proposed for Li batteries [88]. It has good chain flexibility, superior electrochemical stability to lithium ions, a low glass transition temperature, and excellent solubility of lithium salts [89].

The primary downside of current polymer electrolytes is their low conductivity with none being able to reach the 10^{-3} Scm^{-1} of current liquid electrolytes [90]. This lower conductivity has been the subject of intense research over the previous decades [91, 92]. One of the primary questions is the mechanism of ion mobility and how it can be tuned with different material choices. The ethylene oxide groups in PEO form robust solvation shells around Li^{+} cations. While this gives PEO excellent solubility of Li ions, it also complicates the transport of Li ions and leads to a decrease in conductivity. Another aspect limiting the conductivity of polymer electrolytes is their crystal structure [93]. At room temperature, many polymers, including PEO, have both amorphous and crystalline phases coexisting and it is not until the polymer is heated to above its melting point that the entire system switches to a more liquid like disordered phase. Current research suggests that the bulk of the ion transport occurs in the amorphous phase [82]. Because of this limitation, current polymer batteries must operate at temperatures above room temperature to ensure high conductivity [94]. This greatly limits their applications in portable environments and significant research has been conducted to reduce the amount of crystallization

[95, 96]. For our work, we shall simply heat the polymer to above its melting point to a uniform system to measure.

5.2. Polymer electrolytes and heterodyne XPCS

In polymer electrolytes, there are two primary mechanisms for ion transport. The first is segmental motion of the polymer chains that surround the ion [97]. When Li ions are dissolved in PEO, their lowest energy configuration is to form a solvation shell consisting of six ether oxygens coordinating around the Li^+ ion [98]. This segmental motion will result in fluctuations in the polymer matrix. The second is by hopping of the Li^+ ions between occupation sites [99]. The polymer forms a dense entangled matrix where local sites exist. These sites correspond to local energy minima for the ions. The transport of the ions occurs as they hop between these sites [100]. Both of these effects vary depending on temperature, polymer chain length, and salt concentration [101]. These mechanisms determine the performance characteristics of the polymer and a thorough understanding of the fundamental physics that drive each interaction are essential for advancing polymer electrolyte research.

For a polymer electrolyte with univalent salt in a dilute mixture at equilibrium, the current density under an applied potential (ϕ is the potential with respect to the reference electrode) is given by

$$\boldsymbol{i} = -F^2\nabla\phi \sum_{i=+,-} u_i c_i - F \sum_{i=+,-} D_i \nabla c_i + F\boldsymbol{v} \sum_{i=+,-} c_i \qquad (5.1)$$

where u_i is the ion mobility, D_i is the diffusion coefficient, c_i is the ionic concentration, F is Faraday's constant, $\boldsymbol{v}$ is the bulk velocity of the electrolyte, and the sum is taken over all the ionic species [102]. This equation defines the current coming from three separate processes; the current due to ion migration from the applied potential, the current from ion diffusion in a concentration gradient, and the current from convection of the ions. The last term is typically zero for polymer electrolytes so we are left with ion migration from the applied potential and diffusion from the concentration gradient. These are defined with two pairs of parameters, the ion mobility and diffusion coefficient for the positive and negative ions. These parameters can be rewritten in terms of transport properties, ionic conductivity (σ), diffusion coefficient (D), and transference number (t^{+})

$$\sigma = -\frac{i}{\nabla\phi} = F(u_{+}c_{+} + u_{-}c_{-}) \ , \qquad D = \frac{u_{+}D_{-} + u_{-}D_{+}}{u_{+} + u_{-}} \ , \qquad t^{+} = \frac{u_{+}}{u_{+} + u_{-}} \qquad (5.2)$$

These quantities can then be used in continuum models to predict the behavior of various polymer electrolyte for use in batteries. Ionic conductivity can be easily measured using AC impedance electrochemistry [103]. The diffusion coefficient can also be measured using electrochemistry with a symmetric cell with reversible electrodes [104]. Both of these quantities can also be measured with pulsed field NMR and show good agreement with theory for PEO LiTFSI systems [105, 106].

The transference number is the fraction of current in an electrolyte carried by a particular ion and is significantly more difficult to measure. In polymer electrolytes, Li typically has a transference number below 0.5 and means that most of the current carried through the battery is actually moved by the counter-ion [107, 108]. This is because there is strong preference for solvation of Li_+ over the TFSI counterion. This large solvation shell of polymer decreases the mobility of Li_+ in the electrolyte. Because of the low transference number, the system cannot be considered a single ion conductor and the dynamics of both cation and anion must be understood. This leads to electron migration and the formation of a concentration gradient. Because only part of the current is flowing via Li^+ ions, Li is consumed at the positive electrode faster than it is produced by electron migration at the negative electrode. This creates a concentration gradient for the ions and this gradient then causes diffusion of the salt ions that drives the transport of Li^+ that do not participate in electron migration. This concentration gradient can be harmful to battery performance. If it becomes too large, it can cause the salt to precipitate out of solution [109]. Equation 5.1 defines the current for a simplified model with low salt concentration. It is of limited use for functional polymer electrolyte batteries where a much higher salt concentration is required for high performance. Further complicating this are multiple articles showing that transference number is concentration dependent with widespread disagreement in the literature over how to properly measure the transference number, especially in polymer electrolytes [82].

We propose to directly measure the ion velocity and ion concentration using an in-situ polymer cell. These experimental results can then be compared to continuum models of ion transport to provide an experimental verification of transference number [110]. To measure the ion concentration, we collected x-ray absorption scans across the length of the sample. Applying the Lambert-Beer law we can calculate how much the ion concentration has changed due to the applied voltage. We will assume the absorption from the Li is negligible giving terms for the polymer (PEO), the counterion (TFSI), and the sample holder (PEEK)

$$\frac{I}{I_0} = \exp(-\mu_{PEEK} L_{PEEK} C_{PEEK} - \mu_{TFSI} L_{TFSI} C_{TFSI} - \mu_{PEO} L_{PEO} C_{PEO}) \tag{5.3}$$

where μ, L, C represent the attenuation coefficient, x-ray path length, and concentration respectively for each material. We can rearrange to find the concentration of TFSI

$$\exp(-\mu_{TFSI} L_{TFSI} C_{TFSI}) = \frac{I}{I_0 \exp(-\mu_{PEEK} L_{PEEK} C_{PEEK} - \mu_{PEO} L_{PEO} C_{PEO})}$$

$$\mu_{TFSI}L_{TFSI}C_{TFSI} = \log\left(\frac{I}{I_0 \exp(-\mu_{PEEK}L_{PEEK}C_{PEEK} - \mu_{PEO}L_{PEO}C_{PEO})}\right)$$

$$C_{TFSI} = -\log\left(\frac{I}{I_0 \exp(-\mu_{PEEK}L_{PEEK}C_{PEEK} - \mu_{PEO}L_{PEO}C_{PEO})}\right) * \frac{1}{\mu_{TFSI}L_{TFSI}} \tag{5.4}$$

Because we are only concerned with the relative change in TFSI ions after the applied voltage, we can calculate the ratio of the cation concentration compared to the initial concentration

$$C_{ratio} = \frac{C_{TFSI}}{C_{TFSI}(t=0)} = \frac{\log\left(\frac{I(t)}{I_0 \exp(-\mu_{PEEK}L_{PEEK}C_{PEEK} - \mu_{PEO}L_{PEO}C_{PEO})}\right)}{\log\left(\frac{I(t=0)}{I_0 \exp(-\mu_{PEEK}L_{PEEK}C_{PEEK} - \mu_{PEO}L_{PEO}C_{PEO})}\right)} \tag{5.5}$$

We calculated the attenuation coefficients using the CXRO database of atom factors and known densities. Due to the larger absorption cross section of the heavier elements in TFSI, it accounts for 76% of the sample's total absorption. This gives us good sensitivity to changes in its concentration. Using this formalism, we were able to measure the ion concentration in-situ while we applied voltage to the cell.

To measure the velocity of the ions, we used a variation of XPCS called heterodyne detection. A uniform undamped drift velocity $\boldsymbol{v}$ of an ion yields an intermediate scattering function which is of the form $g_1(\boldsymbol{Q}, t) = \exp\,(i\boldsymbol{Q} \cdot \boldsymbol{v}\, t)$ and hence a normal homodyne XPCS experiment, which measures the modulus-squared of this function, would yield no time dependence. To observe this constant velocity motion, we must interfere the ion's scattering signal with a static reference signal [111]. This interference can then be measured to determine how much the ions are moving relative to the static reference signal.

We can generalize the homodyne XPCS formalism from the previous chapter to work out the scattering signal for a heterodyne experiment. The intermediate scattering function for a heterodyne experiment becomes

$$g_{1h}(\boldsymbol{Q},t) = \left(hg_{1s}(\boldsymbol{Q},t) + (1-h)g_{1r}(\boldsymbol{Q},t)\right) \tag{5.6}$$

where h is the heterodyne mixing fraction defined by $h = I_s/(I_s + I_h)$, g_{1s} is the scattering from the sample, and g_{1r} is the scattering from the reference [112]. Using the Siegert relation from the previous chapter gives

$$\begin{aligned} g_{2h}(\boldsymbol{Q},t) &= 1 + \beta\, |g_{1h}(\boldsymbol{Q},t)|^2 \\ &= 1 + \beta[(hg_{1s}^* + (1-h)g_{1r}^*)(hg_{1s} + (1-h)g_{1r})] \\ &= 1 + \beta[h^2|g_{1s}|^2 + \{h(1-h)g_{1s}^*g_{1r} + h(1-h)g_{1s}g_{1r}^*\} + (1-h)^2|g_{1r}|^2] \\ &= 1 + \beta[h^2|g_{1s}|^2 + 2h(1-h)Re(g_{1s}^*g_{1r}) + (1-h)^2|g_{1r}|^2] \end{aligned} \tag{5.7}$$

The first term is the normal homodyne scattering of the sample, the second term is the interference term between the two signals, and the third is the reference scattering. The reference signal is static and therefore the correlation function g_{1r} is unity, giving the final expression for the heterodyne correlation function.

$$g_{2h}(\boldsymbol{Q},t) = 1 + \beta\left[h^2|g_1(\boldsymbol{Q},t)|^2 + 2h(1-h)Re\left(g_1(\boldsymbol{Q},t)\right) + (1-h)^2\right] \tag{5.8}$$

There are several forms for $g_1(\boldsymbol{Q},t)$ that can be used to describe different kinds of particle motion. We chose to use a model with a uniform velocity $\boldsymbol{v}$ and compressed exponential damping term. This form is commonly seen in polymer systems [21]

$$g_1(\boldsymbol{Q},t) = \exp(i\boldsymbol{Q}\cdot\boldsymbol{v}\,t) * \exp\left(-\left(\frac{t}{\tau}\right)^{\gamma}\right) \tag{5.9}$$

Substituting this expression for $g_1(\boldsymbol{Q},t)$ into equation 5.8 gives the complete heterodyne scattering formula

$$g_{2h}(\boldsymbol{Q},t) = 1 + \beta\left[h^2\left|\exp\left(-\left(\frac{t}{\tau}\right)^{\gamma}\right)\right|^2 + 2h(1-h)\cos(\mathbf{Q}\cdot\mathbf{v}\,\mathrm{t})\exp\left(-\left(\frac{t}{\tau}\right)^{\gamma}\right) + (1-h)^2\right]$$

$$g_{2h}(\boldsymbol{Q},t) = 1 + \beta\left[h^2 \exp\left(-2\left(\frac{t}{\tau}\right)^{\gamma}\right) + 2h(1-h)\cos(\omega\, t)\exp\left(-\left(\frac{t}{\tau}\right)^{\gamma}\right) + (1-h)^2\right] \quad (5.10)$$

as a damped oscillatory g_{2h} function where we can define $\omega = \boldsymbol{Q}\cdot\boldsymbol{v} = qv\cos(\phi)$ as the frequency of the oscillations. This frequency depends on $|\boldsymbol{Q}|$ and the angle ϕ between the velocity flow direction and $\boldsymbol{Q}$. This expression shows that correlation function will be a damped oscillation where the frequency scales as a function of ion velocity and the cosine of the angle ϕ. The oscillation frequency is maximum when $\boldsymbol{Q}$ is parallel to the ion velocity and zero when $\boldsymbol{Q}$ is normal. The damping is increased with larger $\boldsymbol{Q}$ values. We can also maximize the oscillation by selecting $h = 0.5$. Using this equation, we can fit the velocity of the ions from the correlation function.

5.3. XPCS and absorption measurements

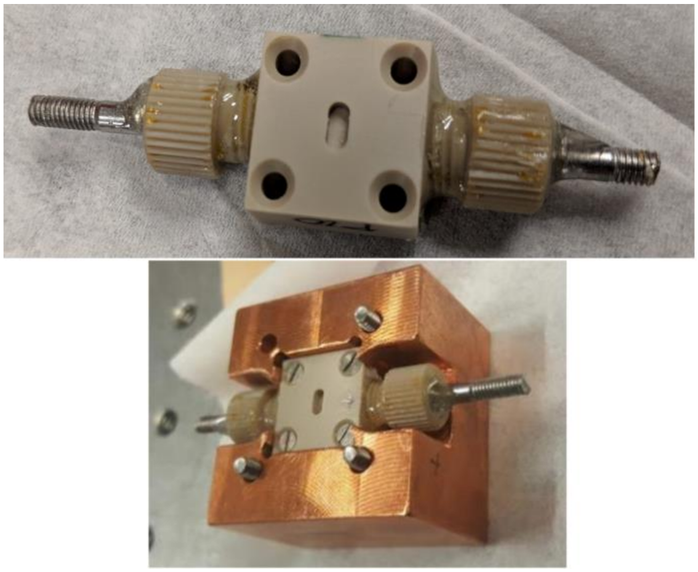

Figure 5.1: Top image shows the sealed electrochemical cell used during measurements. The vertical groove in the center is the x-ray window with the polymer channel oriented horizontally between the screws. Bottom image shows the cell mounted into the copper thermal control block of the beamline.

To measure the velocity using XPCS our collaborators designed a novel electrochemical cell. The cell, pictured in Figure 5.1, was constructed from a block of the inert polymer, polyether ether ketone (PEEK), with a 3 mm long by 1 mm diameter cylindrical channel. PEEK was selected because it's a cheap easily available inert polymer with minimal small angle scattering in the Q range where we measured. The measurements were performed in transmission geometry with the x-ray beam passing normal to the polymer cylinder. Grooves where then machined into the cell to produce windows of PEEK 2 mm thick. These windows would provide the static reference signal needed for heterodyne and the thickness was chosen to maximize the oscillations. On each end of the channel are Li metal electrodes creating a symmetric cell. Into the cell we placed the polymer electrolyte. All handling of the polymer was performed in an argon glove box to prevent moisture from entering the cell.

The specific system we chose was LiTFSI dissolved in 600K PEO. This is a relatively high molecular weight polymer that has a melting point of approximately 60° C. The scattering measurements were taken at two temperatures, 70° C and 90° C. Both of these temperatures are above the melting point and show good conductivity. We measured two different concentrations of ions. The first, which we called P10, has one Li ion and TFSI ion for every ten Ethylene Oxide (EO) monomers. The second, called P6, has one Li ion and TFSI ion for each six EO monomers. The polymers were heated to above their melting point, then the Li and TFSI salts were dissolved into the polymer and allowed to equilibrate. The mixture was then stuffed into the channel in the cell. It was capped with Li metal electrodes at each end and wires were attached to the electrodes. The entire process of creating the cell was performed in the glove box to ensure no moisture contaminated the cells. Multiple samples with each concentration were made to allow different measurements and each sample was labeled with a letter, e.g. P10A.

Unfortunately, because the polymer is highly viscous with such a high concentration of salt, some of our cells developed air bubbles and another one short circuited during the voltage cycling. This meant that some measurements had to be confined to only a small region of the cell and we were unable to measure the velocity at multiple locations along the channel.

Our first experiments with PEO showed highly inconsistent behavior with temperature. We began by measuring a simple homodyne XPCS signal without any applied voltage. These results produced correlation functions with a compressed exponential decay and decay time of around 50 seconds but showed no reproducibility. When the polymer was first heated above its melting point we saw a rapid decrease in the decay time. Then the decay time slowed down over repeated measurements. This slowdown in decay times would last for several hours. If the polymer was cooled below the melting point and then reheated, we measured only slower dynamics with no evidence of the faster decay times. In addition, if the polymers were heated to a higher temperature than had been previously measured, we would once again see a transient fast behavior followed by a gradual slowing of the dynamics. This demonstrated that the polymer dynamics had a complex dependence on temperature and that the temperature history of the sample could not be ignored. We therefore developed the following procedure. Before being measured, the samples were placed on a hot plate to anneal at the maximum temperature we planned to measure at, usually 90° C. Next, the samples were placed in the beamline and heated to 90° C and allowed to equilibrate. During this equilibration, XPCS measurements were being performed to measure the dynamics to determine when the polymer at reached equilibrium. This process typically took a couple of hours. Finally, the voltage was applied and the heterodyne velocity measurements were performed.

The measurements were performed at beamline 8-ID-I of the Advanced Photon Source. We used 11.9 keV x-rays to minimize the damage to the polymer. The beamline was configured to have 10 micron by 10 micron spot size. While, this smaller spot size sacrificed some overall intensity, it produced a higher maximum beamline contrast of 12%. The detector used was a Lambda photon-counting hybrid pixel detector developed by X-Spectrum. It has a minimum readout time of 0.5 milliseconds with large 1556 by 516 pixel array that allowed us to capture the full small angle x-ray scattering pattern from $Q = 3 - 20 \times 10^{-3}$ Å^{-1} with high time resolution. From our earlier temperature stability measurements, we knew the decay time was on the order of tens of seconds. To ensure that we could capture the dynamics on a variety of time scales, we measured every scan with an exposure time 0.3 seconds for 1200 frames giving a total measurement time of 360 seconds. This was repeated for many hours while the voltage applied to the cell was changed. For one of the samples, we also measured the x-ray absorption. After every fifth XPCS measurement, we measured the x-ray absorption by scanning across the sample to determine the ion concentration.

Polymers are notoriously sensitive to x-ray damage and this can easily create dynamics in the system if the total x-ray fluence is too high. We performed a careful series of exposures on a test cell. We varied the attenuation and measured for 1000 seconds; then compared the time decay in each 200 second interval to ensure that the dynamics were stable. Once the appropriate attenuation was determined we created a program to ensure that each individual XPCS measurement was performed on a fresh spot in the polymer. This was done to ensure that the cumulative x-ray dose was never high enough to cause polymer damage driven dynamics. Because the ion dynamics are dependent on the horizontal position in the channel measurements were performed in vertical lines along the channel.

Once all the x-ray scan parameters were calibrated, we began the electrochemistry. The procedure used allowed each cell to thermally equilibrate at open current voltage for at least two hours. During this time the dynamics were monitored with XPCS. After it stabilized, a constant voltage was applied to the cell using Bio-Logic SP150 potentiostat (BioLogic Science Instruments, France). This device would simultaneously measure the output current from the cell while applying a constant voltage. Normal operational performance for these LiTFSI PEO cells is for the current to jump sharply as the voltage is initially applied and then decay with time. This decay would typically take several hours depending on the applied voltage, temperature, and salt concentration. When the applied voltage was turned off, the battery produces no current but it does have an internal voltage called open circuit voltage (OCV). This OCV depends on the voltage history of the cell and will gradually decay with time. If there was a mechanical or electrochemical fault with the cell, such as a void forming or short circuit, this would result in a discontinuous jump in the current. This allowed us to monitor the health of the cell while it was being measured. For the results presented below, we applied multiple voltages to measure their effect on the ion velocity. Between each applied voltage, the OCV of the cell was measured for several hours while the internal dynamics returned to equilibrium.

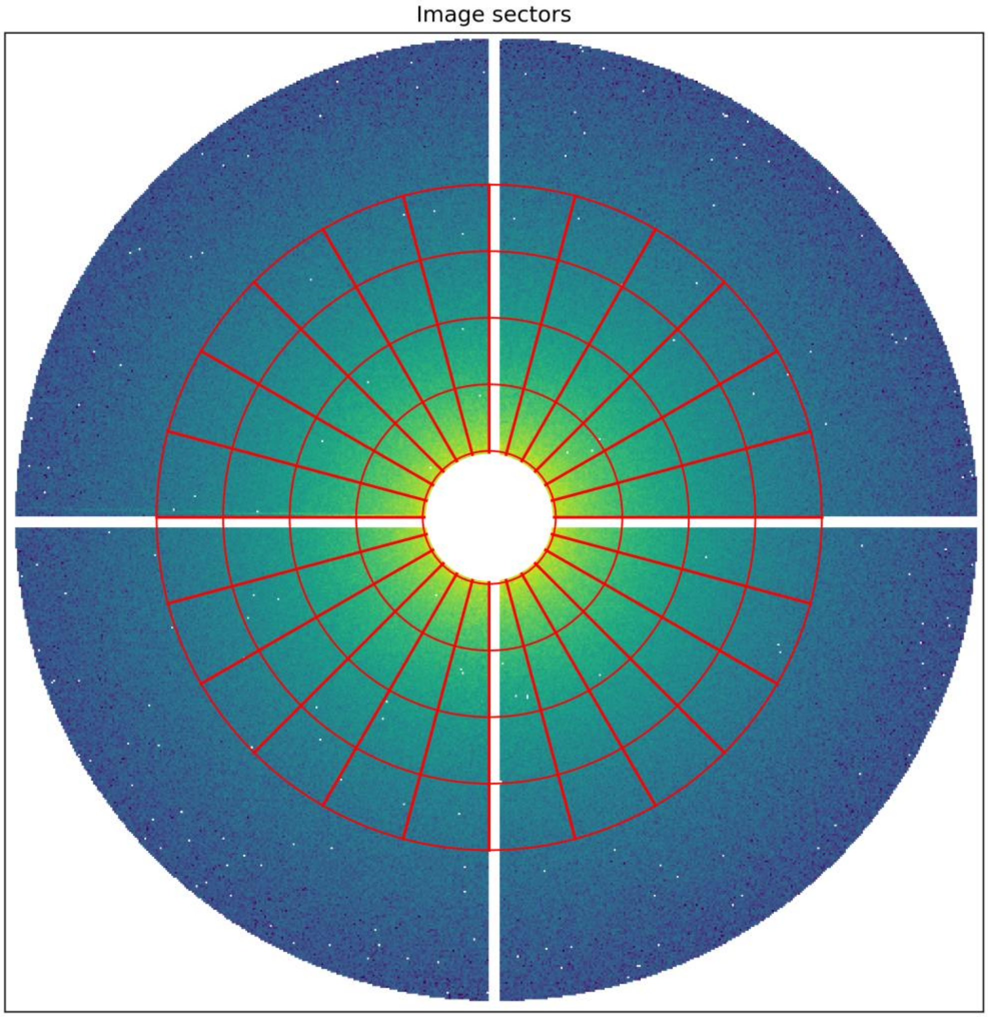

Figure 5.2: Radial and angular divisions of the scattering pattern used to calculate correlation functions.

After the x-ray scattering patterns where measured we computed their correlation functions. This process was performed using XPCSGUI software [113]. As demonstrating in the previous section, the correlation function for heterodyne XPCS is anisotropic and depends on the angle between the ion's velocity and the scattering vector. The correlation function is a dampened oscillation whose frequency depends on the cosine of the angle and the magnitude of Q. To properly capture these dynamics, the image area was divided into 18 angular wedges each subtending 20°. Each wedge was then divided into 9 concentric rings each covering approximately 9×10^{-3} Å^{-1}. Of these 9 rings, only the first 4 rings proved to have sufficient statistical quality to be used for analysis (see Figure 5.2). This created 72 sectors over which the correlation functions were calculated. The correlation functions were first computed using the two-time numerical method and then converted to a normal one-time $g_2(Q, \phi, t)$. This was done for two reasons. First, by calculating the two-time matrix we were able to ensure that the time dynamics did not change over the measurement interval. Second, the logarithmic binning from the multi-tau algorithm can average out an oscillating correlation function. This process resulted in a series of correlation functions for each six-minute interval of the voltage.

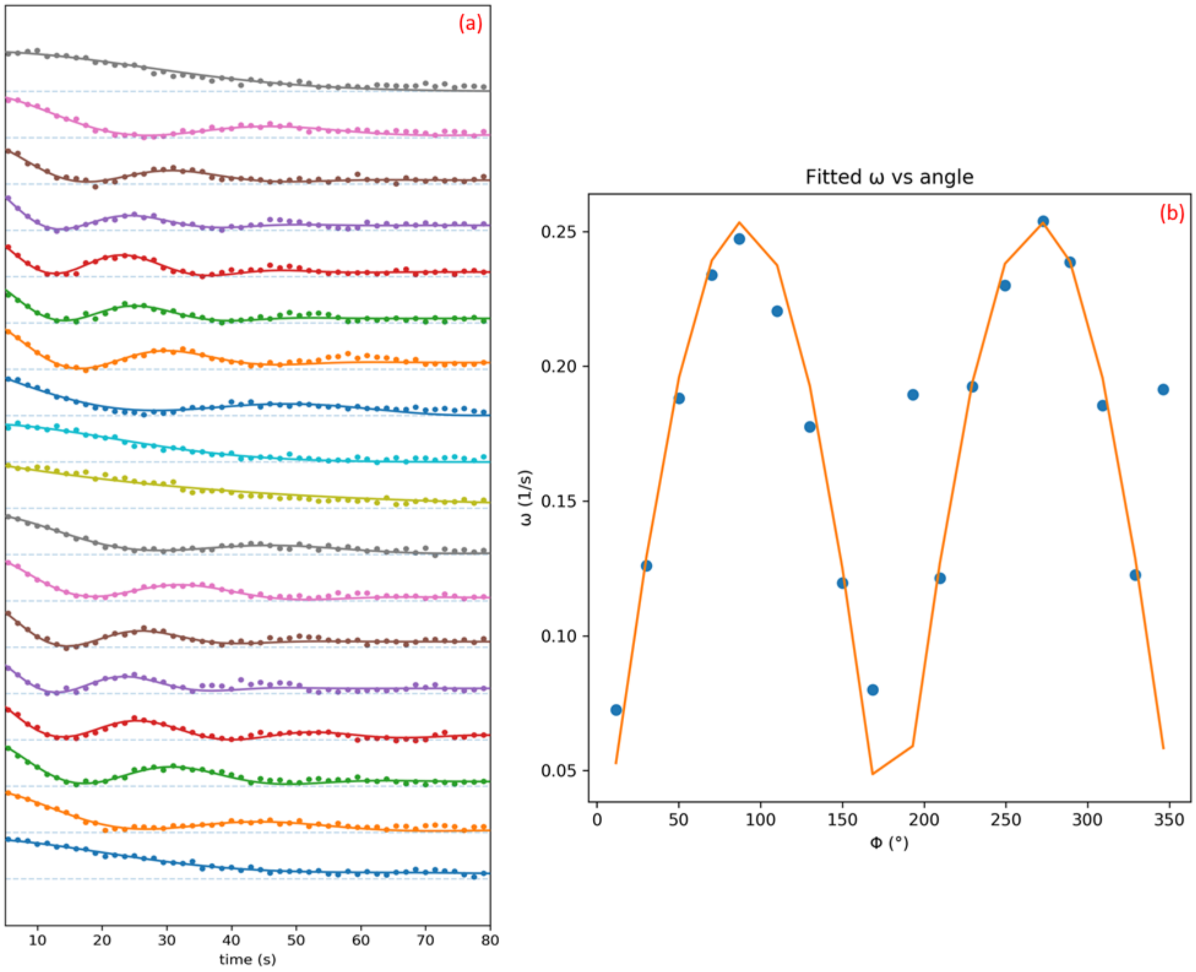

Figure 5.3: (a) Correlation functions at every angle fitted with heterodyne function. (b) Fitted omega as function of angle showing $|\cos \phi|$ dependence

We first analyzed these correlation functions to ensure they matched the heterodyne correlation function shown in the previous section. For each sample, a test scan with clear oscillations was used. Each of the 18 angular sectors in the smallest Q ring was fit individually (see Figure 5.3a). The oscillation frequency (ω) from each these results was then plotted against the scattering angle and fit to $\omega = |\boldsymbol{Q}| \cdot v\ |\cos\phi|$. Our fit showed good agreement with the heterodyne theory and allowed us to measure the ion velocity (see Figure 5.3b). Unfortunately, this fitting procedure was very brittle and required many parameters to be tuned manually to achieve acceptable fits. This proved near impossible for low ion velocities where the oscillation frequency was so low that the correlation function had decayed to baseline before the first oscillation occurred. Furthermore, having over one hundred functions meant that trying to fit them all simultaneously was numerically impossible. The poor numerical stability was primarily caused by the small regions of interest used to create the correlation functions. Because the image had to be divided into so many angular sectors to avoid smearing out the oscillations, each sector had relatively few pixels and was highly noisy.

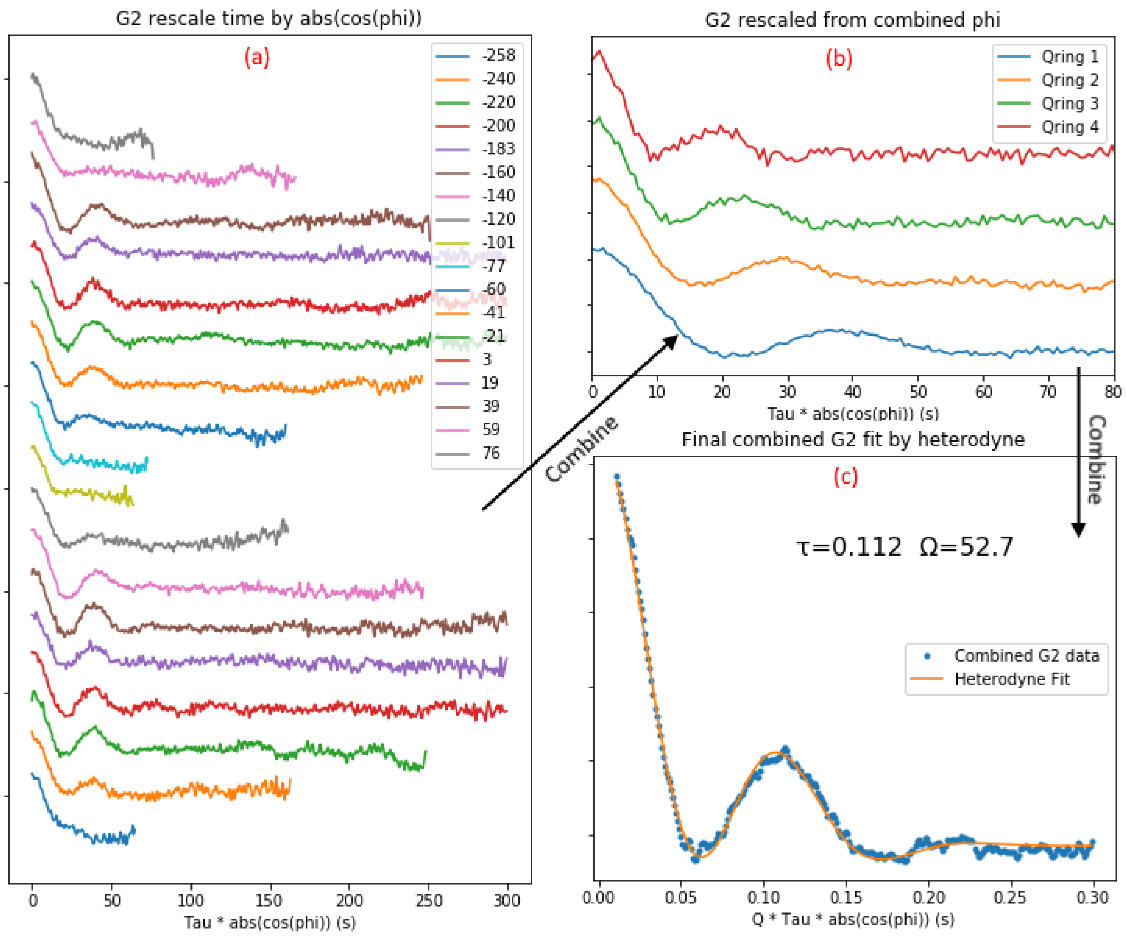

Figure 5.4: Visual overview of the heterodyne fitting process. (a) Each correlation function scaled by $|\cos\phi|$. (b) For each Q ring, the scaled correlation functions are combined. (c) Each Q ring is then scaled by $|Q|$ and combined to create a final correlation function. This correlation function is then fit with the heterodyne scattering formula to get the velocity (Ω)

To overcome the large noise in individual correlation functions, we developed a data processing pipeline that could combine all the correlation functions for a single scan into an overall result and then fit the heterodyne function. First, we group all the correlation functions with the same Q value. Each function is then scaled by $|\cos\phi|$ (see Figure 5.4a). This removes the angular dependence and gives each correlation function the same oscillation frequency. These functions are then summed to produce a single correlation function for each Q value (see Figure 5.4b). The final step involves scaling these combined correlation functions by their Q

value. Because of the noise increases with larger Q, only the first four Q rings were used. This produces an overall combined correlation function that incorporates data from every angle and multiple Q values (see Figure 5.4c). Due to the much larger amount of data, the correlation function is considerately less noisy. This function is then fit to the heterodyne equation. Because the Q and ϕ dependence has been removed, the fitted ω value is the ion velocity.

5.4. Experimental results

The standard model of polymer electrolytes under a constant potential predicts the formation of an ion concentration gradient [114]. This is because the transference number is less than one and therefore some fraction of the current must be carried by the TFSI ions. As time passes, the TFSI ion's concentration increases at the positive electrode and due to electroneutrality a corresponding decrease in Li ion's concentration occurs at the negative electrode. This concentration gradient has three main effects [115]. First, the high concentration causes a diffusive force that opposes additional anionic motion. Second, the ions create an opposite internal voltage that screens out the applied voltage and reduces ion migration. Third, the decrease of Li_+ ions at the negative electrode slows the speed of electron migration. These effects combine to limit the rate of Li transport through the cell with time. Our results confirm this model and show a decaying velocity with time. The initial measured ion velocity starts high and decays as the concentration gradient is created. When the voltage is turned off, we see a very low velocity as diffusion causes the ions to return to a uniform concentration. This process is much slower than the voltage driven transport. Because of the limited intensity that could be used on the polymer, these slower velocities frequently produced correlation functions with no oscillations in the Q range we measured. This leads to a minimum ion velocity that we were able to measure of around 10 Å/s.

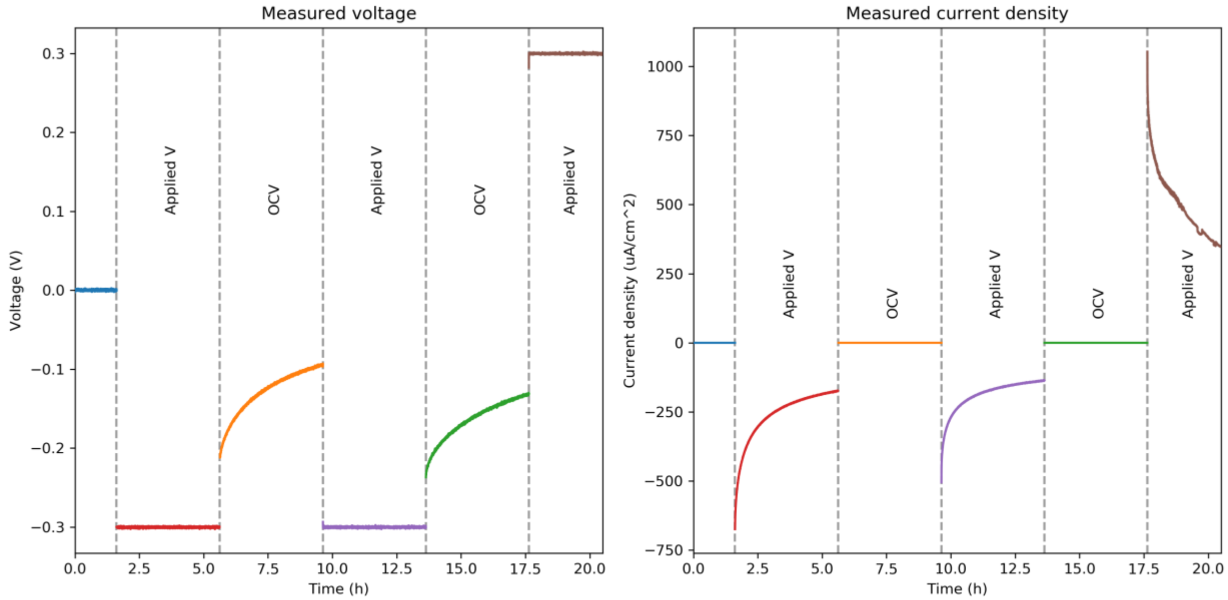

Figure 5.5: Electrochemistry cycling for sample P10B. Alternating periods of applied constant voltage and open circuit voltage were applied. The left pane shows the voltage response and the right pane shows the current response.

Our first results are from sample P10B. This sample has 10 EO to 1 LiTFSI and all measurements were conducted at 90° C. The applied electrochemistry is shown in Figure 5.5. First, the sample was allowed to equilibrate with no applied voltage for several hours. Then -0.3 V were applied for approximately 5 hours. During this time, the current showed a decay as an ion concentration gradient was formed. The voltage was then turned off and the open circuit voltage (OCV) was measured for 4 hours. The voltage during this time also showed a decay as diffusion caused the ion concentration gradient to decrease. Then -0.3 V was applied again for another 4 hours and the current again showed decay. Finally, the voltage was reversed and +0.3 V was applied for 3 hours. This was done to measure the effect of applied voltage on a cell that had already been polarized. While the cell is symmetric with both electrodes being Li, the internal ion concentration gradient created a polarization inside the cell. By applying a constant voltage in the opposite direction, we could observe the ionic transport as both diffusion and electron transport worked to create a reversed ionic concentration. During each of these steps, the XPCS was being measured continuously to determine the velocity of the ion transport. The scan procedure from the previous section was used for the entire process producing over 150 scans. Each one was analyzed to produce the velocity and then compared to the electrochemistry results.

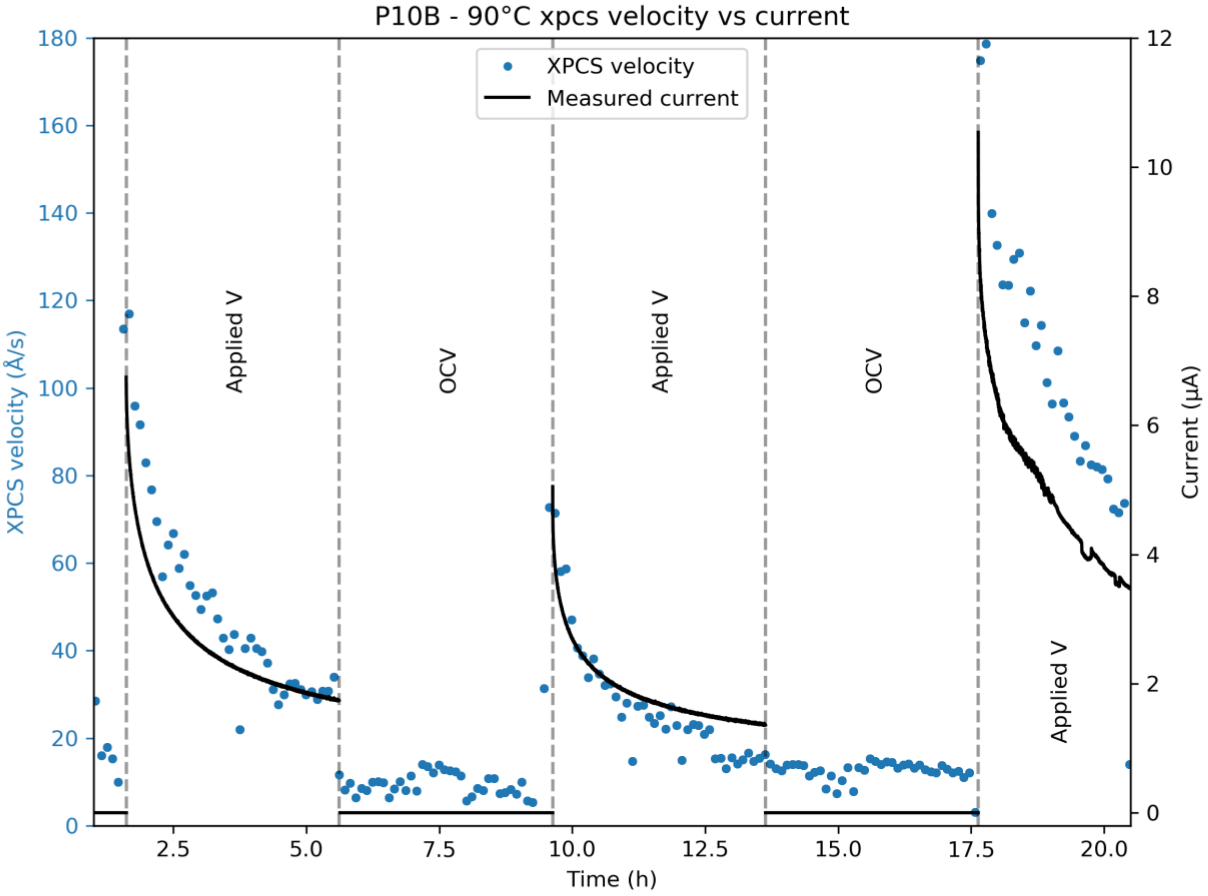

Figure 5.6: Measured XPCS velocity in blue and measured current for P10B in black.

The results for the velocity measured by XPCS show qualitative agreement with the electrochemistry (see Figure 5.6). Each time the voltage is applied, we see an initial spike in the measured velocity that are proportional to the measured current. The first time the voltage is applied, -0.3 V, the starting ion concentration is uniform. The voltage causes a large increase in current which matches the increase in velocity measured with XPCS. As the voltage is applied, an ion concentration gradient is created that screens the applied voltage and decreases the ionic transport of the cell with time. This is reflected in our velocity measurements where the velocity decreases from an initial value of 118 Å/s to down 35 Å/s after 4 hours. When the voltage is turned off, we see the measured velocity drop to around the minimum value we can measure, approximately 10 Å/s. When the voltage is switched on the second time, the initial velocity is lower, 75 Å/s. This is because the four hours of OCV is not enough time for the cell to fully relax and there is still a residual ion concentration gradient. This produces a smaller initial velocity and a faster decay compared to the first applied voltage. During the second OCV, we again see velocities near the minimum measurable value. For the final period, the voltage was applied in the opposite direction, +0.3 V. Because the heterodyne scattering expression depends on the absolute value of the cosine of the velocity angle, it cannot distinguish the direction of the velocity. This reversed applied voltage opposes the residual ion concentration gradient and results in a large increase in current. Our first velocity measurement was 180 Å/s, 50% faster than the first applied voltage. This sizable increase in velocity is caused by diffusion assisting the electron transport. During the first two applied voltages, the internal ion concentration gradient creates an excess of TFSI at the cathode and decreases the concentration of Li at the anode. These concentration gradients create a diffusive pressure that opposes the applied voltage. When the direction of the applied voltage is reversed, this concentration gradient complements the applied voltage and results in a large increase in both current and velocity. After the initial velocity, we see a more rapid and uneven slowdown in velocity compared to the earlier sections.

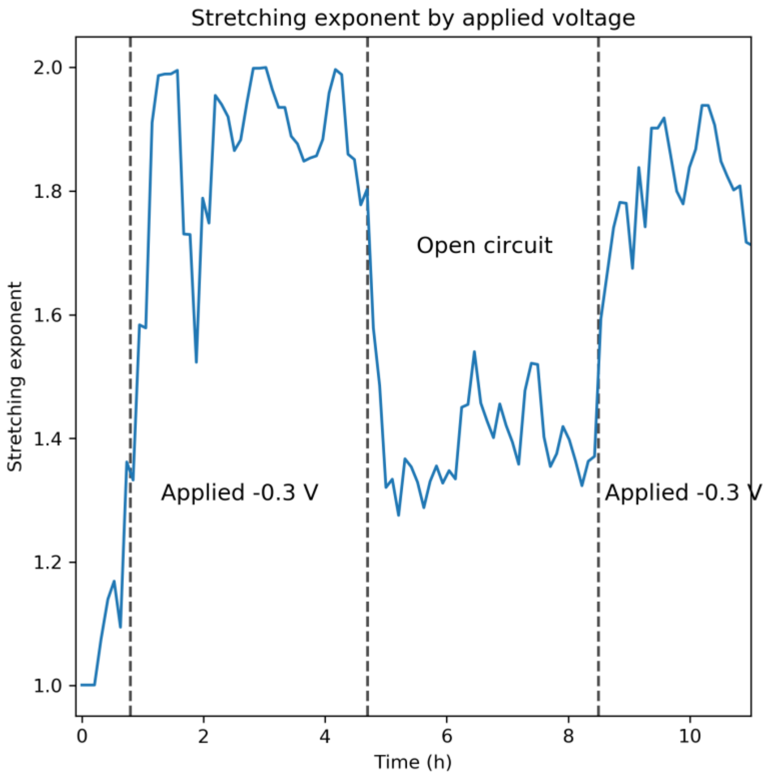

Figure 5.7: Stretching exponent for P10B during applied voltage and OCV.

In addition to fitting the velocity in the heterodyne equation 5.10, we also monitored the stretching exponent. During the applied voltage phases, the stretching exponent increases to near 2. While during the OCV phase, the stretching exponent decreases to around 1.5. These results are characteristic of jamming dynamics commonly seen in polymer systems [116]. The results are quite noisy because the numerical fitting process is relatively insensitive to the stretching exponent given the rapid exponential decay in the oscillations. In follow up experiments, if higher velocities were used and more oscillations were seen in the correlation function, then a more accurate value for the stretching exponent could be obtained.

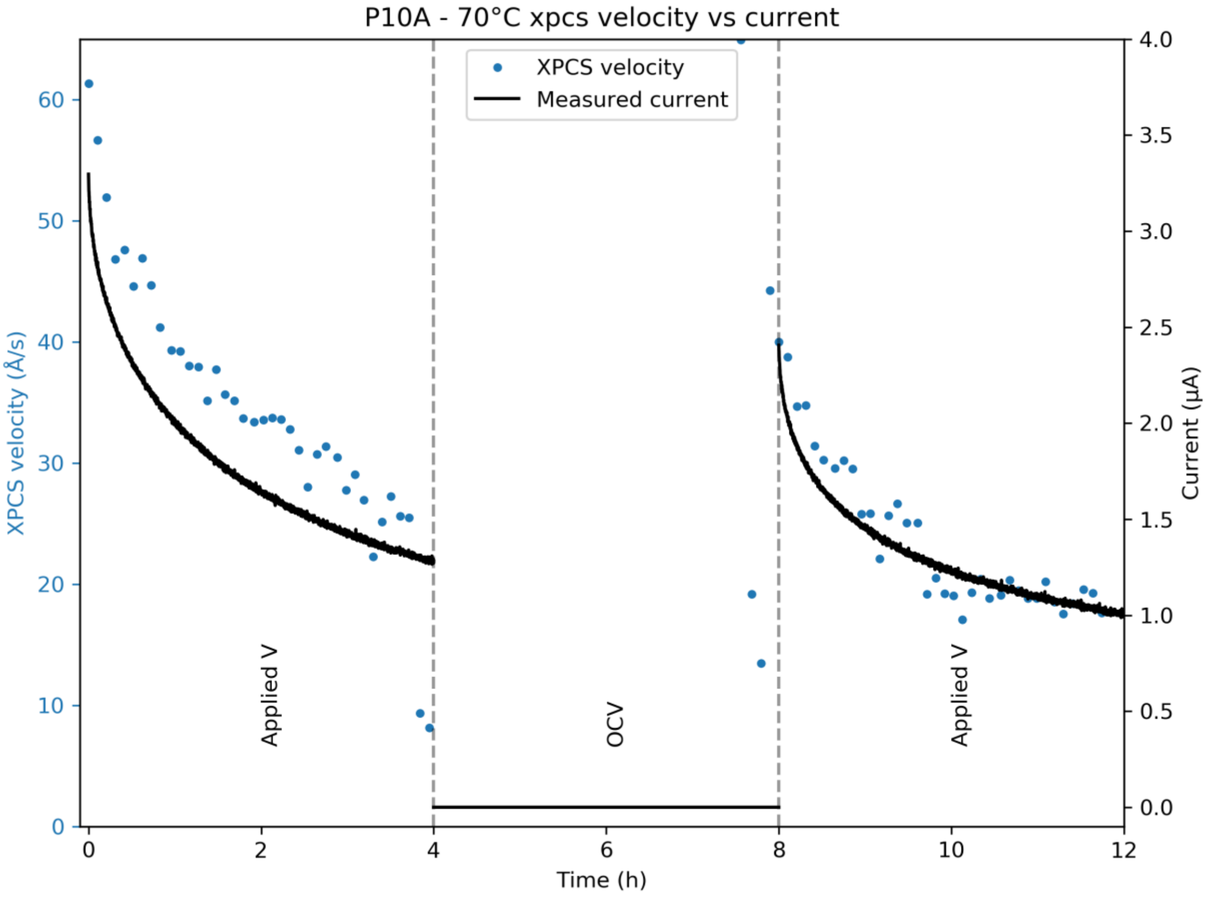

Figure 5.8: Measured XPCS velocity in blue and measured current for P10A at 70° C in black.

Our second measurement was performed on P10A. This sample has the same ion concentration as the previous sample, 10 EO to 1 LiTFSI, and was made from the same batch of polymer. The only difference was that this sample was only heated to a maximum temperature of 70° C. A similar voltage pattern to the previous sample was used. Starting with equilibration, followed by -0.3 V, then OCV, and finally -0.3 V again. Again, the XPCS velocity shows the same basic pattern observed in the 90° C sample (see Figure 5.8). However, the initial velocity of 62 Å/s is much lower than the previous sample. This matches the much lower current measured with the potentiostat and shows the dramatic effect of temperature on the ionic transport. A decrease of 20° C slows the ion mobility by a factor of two. During the OCV phase of this sample, the velocities were too low to be measured and no acceptable fits were obtained. When the voltage was applied the second time, we see a similar pattern to the first sample. The initial velocity of 42 Å/s is lower than the first time and we see a similar decline in velocity as the ion concentration gradient gradually builds in opposition to the applied voltage.

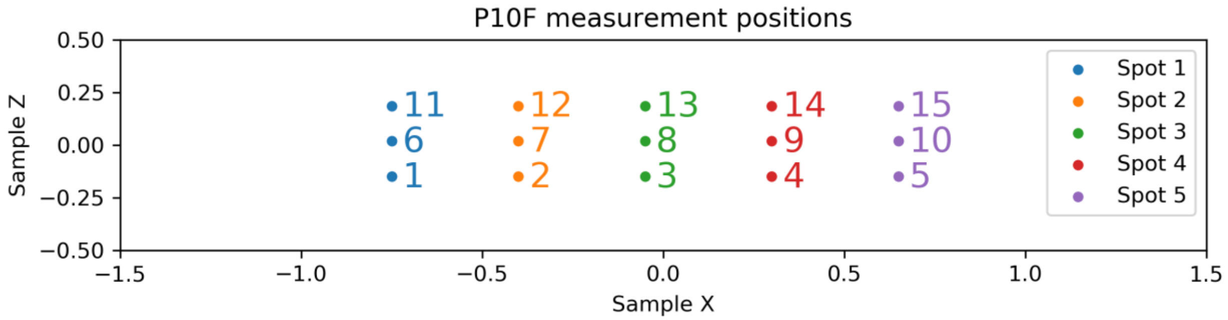

Figure 5.9: Measurement positions for P10F. The sample channel was divided into 5 spots with 1 scan being performed in each region sequentially and then the process repeated. The numbers signify the order of the measurements.

Our final sample was P10F. It also has a ratio of 10 EO to 1 LiTFSI and was measured at 90° C. For this sample, we modified our measurement process. The above results had shown us that a concentration gradient was forming in the cell and its formation was causing the ion velocity to decay as function of time. Several literature sources indicate that the transference number is concentration dependent [117]. We decided to modify our XPCS scans to measure at various points along the cell instead of taking all the measurements at the same area in the center of the cell. This allowed us to determine the velocity distribution as a function of position along the polymer channel. Because each measurement must be performed on a fresh section of polymer to avoid damage, we created a measurement loop. Each loop would measure at one of five spots along the cell, shown as separate colors in Figure 5.9. Then, the x-ray absorption measurement described above would directly measure the concentration of the TFSI. This measurement loop would take approximately 30 minutes. The next loop would offset the positions vertically and remeasure in each of the five spots. This allowed us to track the local velocity of the ions in each region of the cell. For this sample, we allowed the sample to equilibrate at 90° C and then applied -0.3 V. This was the only voltage applied to the cell.

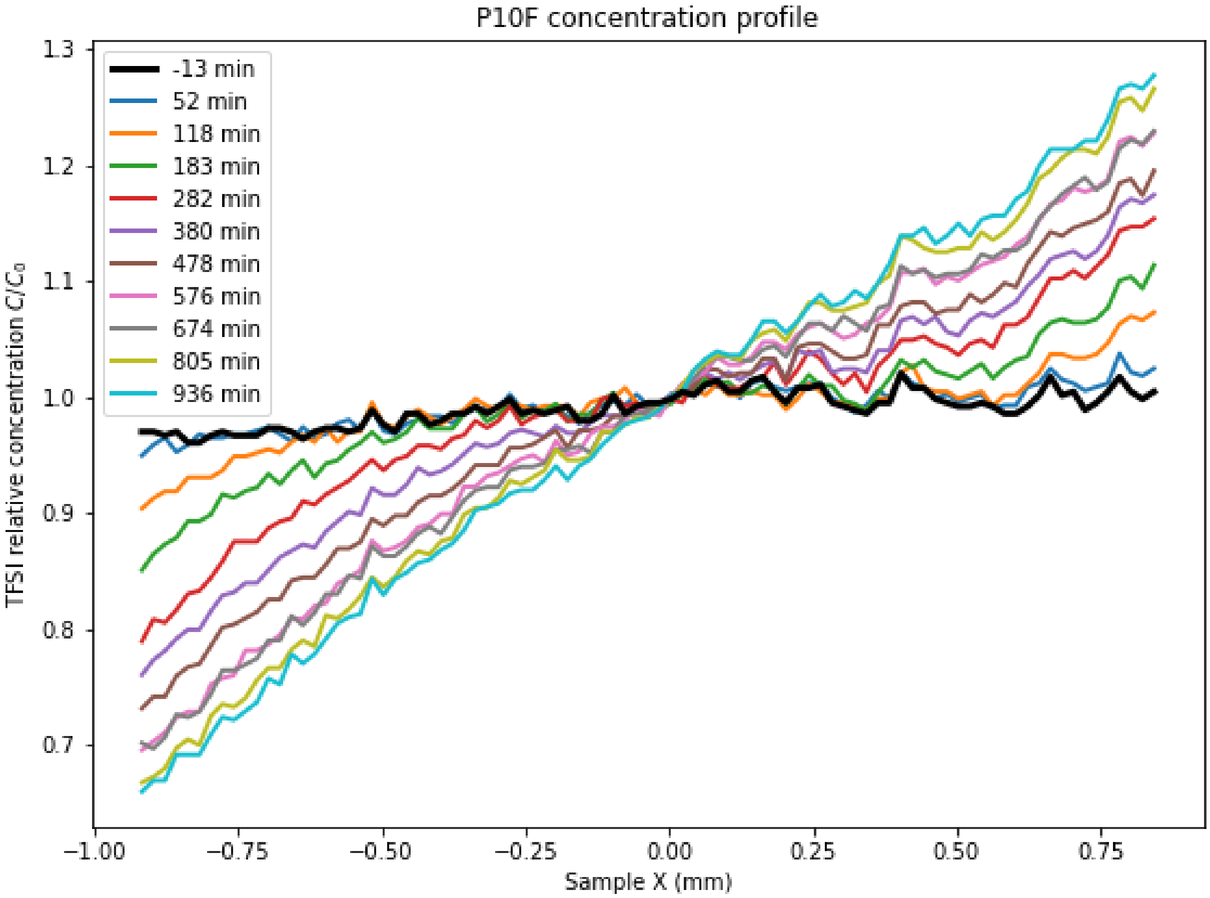

Figure 5.10: TFSI concentration as a function of time for P10F.

In Figure 5.10 we can the TFSI concentration as a function of time. As mentioned in the previous section, these concentrations were calculated by measuring the x-ray absorption and is primarily affected by the concentration of TFSI as it has a much larger scattering cross-section than Li or PEO. Each concentration is compared relative to the initial concentration. Over the first 200 minutes, we see the concentration rise near the anode and decrease near the cathode. This is because the low transference number in the system means that more of the electron transport is being performed by the TFSI. When the TFSI reaches the anode, it cannot be absorbed into the electrode like the Li at the cathode. This causes the TFSI to accumulate at the anode. The concentration profile is not symmetric with a larger change near the anode. After the first 600 minutes, the change in concentration decreases as the cell approaches steady state and the current reaches equilibrium. These results provide direct confirmation of the internal ion concentration gradient formed as voltage is applied to the cell. We can also see that the magnitude of this concentration gradient is quite large with a 35% decrease in TFSI at the cathode. This large concentration gradient resists the transport caused by the applied voltage and increases the internal resistance of the cell. These results provide a direct link between the ion concentration gradient and the steady state internal resistance.

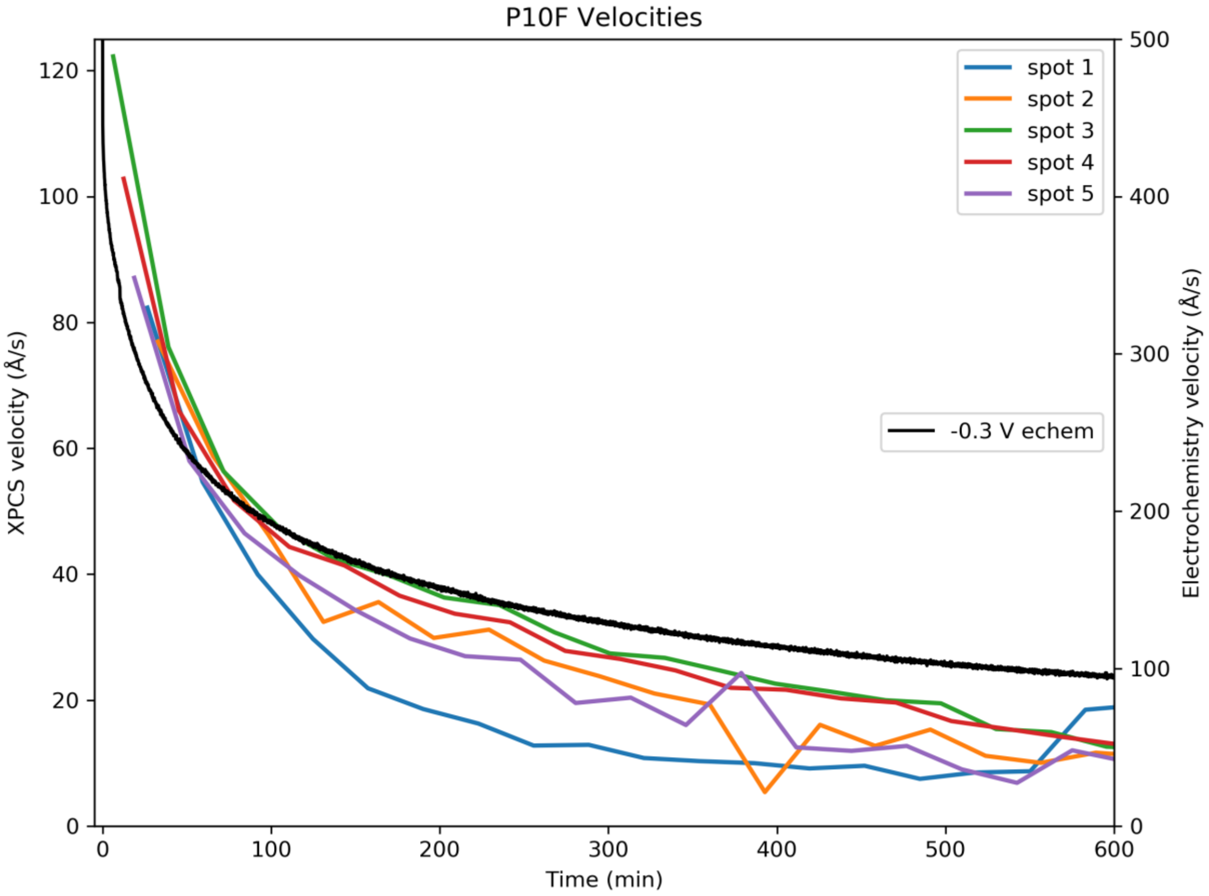

Figure 5.11: Measured XPCS velocity and current for P10F. Velocities were measured at five separate locations along the channel.

In Figure 5.11, the current is plotted as a function of time showing a similar decay pattern to the previous samples. For this plot, we have converted the measured current into an average ion velocity and this is plotted in black on the right axis. This was performed by taking the current measured by the potentiostat and computing an average ion velocity using the size of the channel. The XPCS results show a similar velocity decay to the previous measurements. However, by measuring at different locations we now see a large difference in measured velocity as a function of position. Initially, the velocities are relatively similar across the cell. As time passes and the concentration gradient increases, we see a divergence in velocity as the region near the anode shows slower velocities and the regions near the cathode show a faster velocity. We also see that the velocity measured with XPCS is a factor 3 less, on average, than the velocity calculated from the current.

The velocity calculated from the current is fairly accurate, depending only on the dimensions of the cell. And while it has the same shape as the velocity calculated from XPCS, it's nearly three times larger. The measured Q range used in the heterodyne XPCS is 0.003 to 0.01 Å-1. This corresponds to a length scale of $2\pi/Q \sim 300\ to\ 1000$ Å. In addition, the total scattering intensity is higher on the side of the cell with a lower concentration of TFSI. These facts suggest that the observed scattering has its origin in the larger network structure of the polymer and not the motion of the small TFSI ions. And that the velocity being measured by the heterodyne XPCS is the overall motion of the polymer matrix with respect to the electrodes.

When we polarize the cell, the voltage will lead to a net migration of TFSI ions towards the anode. From an internal perspective, each TFSI ion that moves toward the anode will leave a void. The only compensation mechanism to fill this space is for PEO monomers to move in the opposite direction. Each TFSI ion that moves toward the anode will induce some number of EO monomer to move toward the cathode. The number of EO monomers required to fil the void created by a TFSI ion is proportional the relative volume of each molecule. The molecular volume of ethylene oxide can be obtained from its density and the molecular weight of the polymer. The molecular volume of TFSI was obtained from literature and are $V_{EO} = 65\ \text{Å}^3$ $, V_{TFSI} = 248\ \text{Å}^3$ [118]. From the preparation of the cell, we know that there are 10 EO monomers for each TFSI ion. This gives a total volumetric ratio of

$$V_{EO}:V_{TFSI} = \frac{10 \cdot 65}{248} = 2.6 \tag{5.11}$$

This means that measured XPCS velocity is actually the ensemble average of PEO moving opposite to the TFSI ions. And this velocity should be multiplied by 2.6 to obtain the velocity of the TFSI ions. This shows good agreement with the TFSI ion velocity calculated from the measured current. These results have been compared to continuum modeling of polymer electrolytes and show nice agreement with these more sophisticated theoretical models.

5.5. Conclusions

These measurements are the first of their kind and show direct evidence of the ion transport dynamics inside a polymer electrolyte. They allow the characterizations of in-situ polymer electrolyte performance under a range of voltages and temperatures. Our results demonstrate the first direct measurement of the velocity of ions in-situ in a polymer electrolyte. They clearly show the formation of an ion concentration gradient with applied voltage. By utilizing heterodyne XPCS, we provide direct evidence that the ion velocity matches the measured current of a polymer electrolyte under applied voltage. When the voltage is first applied, the electrochemistry shows a quick spike in output current before gradually decaying to steady state. Our results confirm that the ions velocity follows the same pattern. There is a sharp initial rise in measured velocity proportional to the current that gradually decays to steady state. We have also shown that velocity of the ions is dependent on their position inside the cell with velocity near the anode being around half the velocity near the cathode. This combined with the x-ray absorption measurements that allowed us to measure the TFSI ion concentration across the channel provide direct evidence that the transference number is concentration dependent. This finding has been long suspected by the polymer community but our results provide the first direct observation of this effect. Furthermore, by measuring both the ion velocity and concentration, we can provide experimental validation to continuum models used to understand polymer electrolyte performance.

These results show the utility of heterodyne XPCS for polymer electrolytes and provide several options for follow up measurements. While we planned to measure multiple different salt concentrations, our limited time at the beamline meant we could only measure one sample with the higher salt concentration. Unfortunately, this sample short circuited and we were unable to use the results. For our next beamtime, we plan to measure different salt concentrations to determine their effect on ion velocity. In addition, we plan to use different molecular weight polymers to understand the effect of polymer size on ionic transport. These results would provide valuable information on how different polymer properties effect their ionic transport and would prove invaluable in the quest to engineer high performance battery polymers electrolytes.

The text in Chapter 5 is based on material prepared for submission by

H. G. Steinruck, B. Holladay, C. Takacs, D. Mackanic, H. K. Kim, C. Cao, S. Narayanan, E. Dufresne, Y. Chushkin, B. Ruta, F. Zontone, J. Will, O. Borodin, S. K. Sinha, V. Srinivasan, M. Toney. “Understanding ion transport in polymeric electrolytes via x-ray photon correlation spectroscopy”. The dissertation author was a major contributor to this paper.

Chapter 6. Conclusion

In this dissertation, we presented the results of two different experiments both utilizing coherent x-rays. Each experiment built on the standard methodology of XPCS and extended its capabilities to measure the dynamics of systems that were previously inaccessible. In both of these experiments, numerous technical limitations had to be overcome and extensive testing and validation had to be performed to demonstrate the reliability of our findings. A significant portion of the research work documented here went into creating the tools and algorithms to enable these novel measurement methods. And while the results presented above provide valuable understanding into the dynamics of magnetic skyrmions and polymer electrolytes, the methods developed have great potential for understanding the dynamics in a wide range of systems.

In Chapter 3, we presented the theory underlying two-pulse XPCS and a treatment of magnetic skyrmions. This chapter explained how we could use the statistical properties of x-ray speckle pattern to measure the contrast of the system. By measuring this contrast for the sum of two speckle patterns, we can recover the intermediate scattering function for the time delay between the pulses. Then, this delay time can then be varied to measure $S(\boldsymbol{Q},t)$ for the system. This method is not limited by the speed of the x-ray detector, only the delay times available from the x-ray source. This enabled us to measure the nanosecond dynamics of a magnetic skyrmion lattice. In this chapter, we also presented a treatment of magnetic phases in FeGd multilayers. This included the stripe phase and the hexagonal skyrmion lattice phase. These magnetic phases, and the transition between them, show intriguing dynamics that proved the ideal candidate to test our two-pulse XPCS method.

In Chapter 4, we presented the results from a pair of experiments utilizing this novel two-pulse XPCS technique to measure the dynamics of the magnetic skyrmion lattice in FeGd. Our first experiment was a proof of concept to demonstrate the viability of our method. Numerous technical limitations were overcome. We were able to measure speckle contrast four different time points for the skyrmion lattice phase and the stripe-to-skyrmion transition phase. The skyrmion lattice phase showed an exponential decay with a decay time of 4 ns. The stripe-to-skyrmion transition phase decayed much faster at 300 ps. For the second experiment, we made numerous improvements to the data processing pipeline, detectors, and x-ray source capabilities. This enabled us to measure more data points at four different magnetic fields. These results confirmed the relatively fast exponential decay of the skyrmion lattice. They also showed that both the formation and destruction of this phase had much slower jammed dynamics. These jammed dynamics showed a decay time around 30 ns and evidence of critical behavior. These results provide information about the equilibrium fluctuations of skyrmion lattice that could not be measured with existing techniques. They also show the potential to use the two-pulse method to measure ultrafast dynamics in a wide range of systems using coherent x-rays.

In Chapter 5, we showed direct measurement of the ion velocity in a polymer electrolyte using heterodyne XPCS. Conventional XPCS cannot measure the absolute velocity of ions. By utilizing heterodyning to interfere a static reference signal with the scattering from the sample, we can measure the internal velocity of the ions. This velocity is crucial to understanding the electrochemical properties of polymer electrolytes and their application to battery technology. Our measurements were performed on model system of PEO and LiTFSI performed at multiple temperatures. Under applied voltage, the measured velocity showed an initial spike followed by a gradual decay. This behavior closely matched the measured current produced by the cell. These results provide direct evidence of the formation and strength of an ion concentration gradient being created by the applied voltage in the polymer. This concentration gradient opposes the applied voltage and causes a gradual decrease in the velocity of the ions. In addition, we have shown the effect of temperature on the ion’s velocity. Finally, we have measured the positional dependence of the ion’s velocity and correlated this with the local ion concentration. By providing experimental values for the velocity and concentration for a real battery polymer electrolyte, we have created a valuable dataset for the validation of continuum models to better understand the behavior of polymer electrolytes.

Chapter 7. Bibliography

[1] N. Stribeck, *X-ray scattering of soft matter* (Springer Science & Business Media, 2007).

[2] J. Daillant, A. Gibaud, *X-ray and neutron reflectivity: principles and applications* (Springer, 2008), vol. 770.

[3] C. A. MacDonald, *An Introduction to X-Ray Physics, Optics, and Applications* (Princeton University Press, 2017).

[4] J. J. Thomson, *Conduction of electricity through gases* (Univserity Press, 1903).

[5] S. B. Wilkins, P. D. Hatton, M. D. Roper, D. Prabhakaran, A. T. Boothroyd, Soft x-ray resonant magnetic diffraction. *Phys. Rev. Lett.* 90, 187201 (2003).

[6] D. Gibbs, D. R. Harshman, E. D. Isaacs, D. B. McWhan, D. Mills, C. Vettier, Polarization and Resonance Properties of Magnetic X-Ray Scattering in Holmium. *Phys. Rev. Lett.* 61, 1241–1244 (1988).

[7] J. P. Hannon, G. T. Trammell, M. Blume, D. Gibbs, X-Ray Resonance Exchange Scattering. *Phys. Rev. Lett.* 61, 1245–1248 (1988).

[8] C. Vettier, Resonant x-ray scattering from magnetic materials. *J. Magn. Magn. Mater.* 129, 59–65 (1994).

[9] B. W. J. McNeil, N. R. Thompson, X-ray free-electron lasers. *Nat. Photonics*. 4, 814 (2010).

[10] J. Als-Nielsen, D. McMorrow, *Elements of Modern X-ray Physics: Second Edition* (2011).

[11] M. Sutton, S. G. J. Mochrie, T. Greytak, S. E. Nagler, L. E. Berman, G. A. Held, G. B. Stephenson, Observation of speckle by diffraction with coherent X-rays. *Nature*. 352, 608–610 (1991).

[12] C. Gutt, T. Ghaderi, M. Tolan, S. K. Sinha, G. Grübel, Effects of partial coherence on correlation functions measured by x-ray photon correlation spectroscopy. *Phys. Rev. B*. 77, 94133 (2008).

[13] S. K. Sinha, M. Tolan, A. Gibaud, Effects of partial coherence on the scattering of x rays by matter. *Phys. Rev. B*. 57, 2740 (1998).

[14] D. Lumma, L. B. Lurio, S. G. J. Mochrie, M. Sutton, Area detector based photon correlation in the regime of short data batches: Data reduction for dynamic x-ray scattering. *Rev. Sci. Instrum.* 71, 3274–3289 (2000).

[15] S. K. Sinha, E. B. Sirota, Garoff, S, H. B. Stanley, X-ray and neutron scattering from rough surfaces. *Phys. Rev. B*. 38, 2297 (1988).

[16] B. J. Berne, R. Pecora, *Dynamic light scattering: with applications to chemistry, biology, and physics* (Courier Corporation, 2000).

[17] G. Grübel, F. Zontone, Correlation spectroscopy with coherent X-rays. *J. Alloys Compd.* 362, 3–11 (2004).

[18] O. G. Shpyrko, X-ray photon correlation spectroscopy. *J. Synchrotron Radiat.* 21, 1057–1064 (2014).

[19] E. R. Pike, H. Z. Cummins, *Photon Correlation Spectroscopy and Velocimetry* (Plenum Press, 1977).

[20] H. Kim, A. Rühm, L. B. Lurio, J. K. Basu, J. Lal, D. Lumma, S. G. J. Mochrie, S. K. Sinha, Surface Dynamics of Polymer Films. *Phys. Rev. Lett.* 90, 068302 (2003).

[21] F. Livet, F. Bley, F. Ehrburger-Dolle, I. Morfin, E. Geissler, M. Sutton, X-ray intensity fluctuation spectroscopy by heterodyne detection. *J. Synchrotron Radiat.* 13, 453–458 (2006).

[22] I. Johnson, A. Bergamaschi, J. Buitenhuis, R. Dinapoli, D. Greiffenberg, B. Henrich, T. Ikonen, G. Meier, A. Menzel, A. Mozzanica, others, Capturing dynamics with Eiger, a fast-framing X-ray detector. *J. Synchrotron Radiat.* 19, 1001–1005 (2012).

[23] V. M. Uzdin, M. N. Potkina, I. S. Lobanov, P. F. Bessarab, H. Jónsson, Energy surface and lifetime of magnetic skyrmions. *J. Magn. Magn. Mater.* 459, 236–240 (2018).

[24] X. Z. Yu, Y. Onose, N. Kanazawa, J. H. Park, J. H. Han, Y. Matsui, N. Nagaosa, Y. Tokura, Real-space observation of a two-dimensional skyrmion crystal. *Nature*. 465, 901–904 (2010).

[25] F. Lehmkühler, P. Kwaśniewski, W. Roseker, B. Fischer, M. A. Schroer, K. Tono, T. Katayama, M. Sprung, M. Sikorski, S. Song, J. Glownia, M. Chollet, S. Nelson, A. Robert, C. Gutt, M. Yabashi, T. Ishikawa, G. Grübel, Sequential Single Shot X-ray Photon Correlation Spectroscopy at the SACLA Free Electron Laser. *Sci. Rep.* 5, 17193 (2015).

[26] H. Y. Yuan, X. R. Wang, Skyrmion creation and manipulation by nano-second current pulses. *Sci. Rep.* 6, 22638 (2016).

[27] C. Gutt, L.-M. Stadler, A. Duri, T. Autenrieth, O. Leupold, Y. Chushkin, G. Grübel, Measuring temporal speckle correlations at ultrafast x-ray sources. *Opt. Express*. 17, 55 (2009).

[28] P. K. Dixon, D. D.-P. review Letters, U. 2003, D. J. Durian, Speckle Visibility Spectroscopy and Variable Granular Fluidization. *Phys. Rev. Lett.* (2003).

[29] E. Miyata, M. Miki, J. Hiraga, D. Kamiyama, H. Kouno, H. Tsunemi, K. Miyaguchi, K. Yamamoto, Mesh experiment for back-illuminated CCDs in improvement of position resolution. *Nucl. Instruments Methods Phys. Res. Sect. A Accel. Spectrometers, Detect.*

Assoc. Equip. 513, 322–326 (2003).

[30] F. Livet, F. Bley, J. Mainville, R. Caudron, S. G. J. Mochrie, E. Geissler, G. Dolino, D. Abernathy, G. Grübel, M. Sutton, Using direct illumination CCDs as high-resolution area detectors for X-ray scattering. *Nucl. Instruments Methods Phys. Res. Sect. A Accel. Spectrometers, Detect. Assoc. Equip.* 451, 596–609 (2000).

[31] J. W. Goodman, *Speckle phenomena in optics: theory and applications* (Roberts and Company Publishers, 2007).

[32] J. W. Goodman, *Statistical optics* (John Wiley & Sons, 1985).

[33] R. Bandyopadhyay, A. S. Gittings, S. S. Suh, P. K. Dixon, D. J. Durian, Speckle-visibility spectroscopy: A tool to study time-varying dynamics. *Rev. Sci. Instrum.* 76, 93110 (2005).

[34] M. Sikorski, S. Song, A. Schropp, F. Seiboth, Y. Feng, R. Alonso-Mori, M. Chollet, H. T. Lemke, D. Sokaras, T.-C. Weng, W. Zhang, A. Robert, D. Zhu, Focus characterization at an X-ray free-electron laser by coherent scattering and speckle analysis. *J. Synchrotron Radiat.* 22, 599–605 (2015).

[35] C. Ponchut, Correction of the charge sharing in photon-counting pixel detector data. *Nucl. Instruments Methods Phys. Res. Sect. A Accel. Spectrometers, Detect. Assoc. Equip.* 591, 311–313 (2008).

[36] J. Möller, M. Reiser, J. Hallmann, U. Boesenberg, A. Zozulya, H. Rahmann, A.-L. Becker, F. Westermeier, T. Zinn, F. Zontone, C. Gutt, A. Madsen, IUCr, Implications of disturbed photon-counting statistics of Eiger detectors for X-ray speckle visibility experiments. *J. Synchrotron Radiat.* 26, 1705–1715 (2019).

[37] Y. Chushkin, C. Caronna, A. Madsen, IUCr, A novel event correlation scheme for X-ray photon correlation spectroscopy. *J. Appl. Crystallogr.* 45, 807–813 (2012).

[38] F. J. Decker, W. Colocho, Z. Huang, R. Iverson, A. Krasnykh, A. Lutman, M. Nguyen, T. Raubenheimer, M. Ross, J. L. Turner, others, in *FEL Proceedings, editor, Proc. 36 th Int. Free-Electron Laser Conf., New York* (2013).

[39] S. A. Montoya, S. Couture, J. J. Chess, J. C. T. Lee, N. Kent, D. Henze, S. K. Sinha, M. Y. Im, S. D. Kevan, P. Fischer, B. J. McMorran, V. Lomakin, S. Roy, E. E. Fullerton, Tailoring magnetic energies to form dipole skyrmions and skyrmion lattices. *Phys. Rev. B*, 024415 (2017).

[40] X. Yu, J. P. DeGrave, Y. Hara, T. Hara, S. Jin, Y. Tokura, Observation of the Magnetic Skyrmion Lattice in a MnSi Nanowire by Lorentz TEM. *Nano Lett.* 13, 3755–3759 (2013).

[41] W. Münzer, A. Neubauer, T. Adams, S. Mühlbauer, C. Franz, F. Jonietz, R. Georgii, P. Böni, B. Pedersen, M. Schmidt, A. Rosch, C. Pfleiderer, Skyrmion lattice in the doped semiconductor Fe_{1-x} Co_x Si. *Phys. Rev. B.* 81, 041203 (2010).

[42] J. Chess, S. Montoya, J. Lee, S. Roy, S. Kevan, E. Fullerton, B. McMorran, Observation of Skyrmions at Room-temperature in Amorphous Fe/Gd Films. *Microsc. Microanal.* 21, 1649–1650 (2015).

[43] M. Garst, J. Waizner, D. Grundler, Collective spin excitations of helices and magnetic skyrmions: review and perspectives of magnonics in non-centrosymmetric magnets. *J. Phys. D. Appl. Phys.* 50, 293002 (2017).

[44] A. Singh, M. K. Sanyal, J. C. T. Lee, Y. Chen, S. Montoya, E. E. Fullerton, S. Roy, in *AIP Conference Proceedings* (AIP Publishing LLC, 2018), vol. 1942, p. 130028.

[45] F. Radu, R. Abrudan, I. Radu, D. Schmitz, H. Zabel, Perpendicular exchange bias in ferrimagnetic spin valves. *Nat. Commun.* 3, 715 (2012).

[46] H. Oike, A. Kikkawa, N. Kanazawa, Y. Taguchi, M. Kawasaki, Y. Tokura, F. Kagawa, Interplay between topological and thermodynamic stability in a metastable magnetic skyrmion lattice. *Nat. Phys.* 12, 62 (2016).

[47] K. Chesnel, J. J. Turner, M. Pfeifer, S. D. Kevan, Probing complex materials with coherent soft X-rays. *Appl. Phys. A.* 92, 431–437 (2008).

[48] J. C. T. Lee, J. J. Chess, S. A. Montoya, X. Shi, N. Tamura, S. K. Mishra, P. Fischer, B. J. McMorran, S. K. Sinha, E. E. Fullerton, S. D. Kevan, S. Roy, Synthesizing skyrmion bound pairs in Fe-Gd thin films. *Appl. Phys. Lett.* 109, 022402 (2016).

[49] D. McGrouther, R. J. Lamb, M. Krajnak, S. McFadzean, S. McVitie, R. L. Stamps, A. O. Leonov, A. N. Bogdanov, Y. Togawa, Internal structure of hexagonal skyrmion lattices in cubic helimagnets. *New J. Phys.* 18, 095004 (2016).

[50] A. Singh, J. C. T. Lee, K. E. Avila, Y. Chen, S. A. Montoya, E. E. Fullerton, P. Fischer, K. A. Dahmen, S. D. Kevan, M. K. Sanyal, S. Roy, Scaling of domain cascades in stripe and skyrmion phases. *Nat. Commun.* 10, 1988 (2019).

[51] F. Büttner, M. Kläui, in *Skyrmions* (CRC Press, 2016).

[52] S. Mühlbauer, B. Binz, F. Jonietz, C. Pfleiderer, A. Rosch, A. Neubauer, R. Georgii, P. Böni, Skyrmion lattice in a chiral magnet. *Science (80-.).* 323, 915–919 (2009).

[53] A. O. Leonov, T. L. Monchesky, N. Romming, A. Kubetzka, A. N. Bogdanov, R. Wiesendanger, The properties of isolated chiral skyrmions in thin magnetic films. *New J. Phys.* 18, 065003 (2016).

[54] J. Sampaio, V. Cros, S. Rohart, A. Thiaville, A. Fert, Nucleation, stability and current-induced motion of isolated magnetic skyrmions in nanostructures. *Nat. Nanotechnol.* 8, 839–844 (2013).

[55] N. S. Kiselev, A. N. Bogdanov, R. Schäfer, U. K. Rößler, Chiral skyrmions in thin magnetic films: new objects for magnetic storage technologies? *J. Phys. D. Appl. Phys.*

44, 392001 (2011).

[56] C. Bostedt, S. Boutet, D. M. Fritz, Z. Huang, H. J. Lee, H. T. Lemke, A. Robert, W. F. Schlotter, J. J. Turner, G. J. Williams, Linac Coherent Light Source: The first five years. *Rev. Mod. Phys.* 88, 015007 (2016).

[57] P. Heimann, O. Krupin, W. F. Schlotter, J. Turner, J. Krzywinski, F. Sorgenfrei, M. Messerschmidt, D. Bernstein, J. Chalupský, V. Hájková, S. Hau-Riege, M. Holmes, L. Juha, N. Kelez, J. Lüning, D. Nordlund, M. Fernandez Perea, A. Scherz, R. Soufli, W. Wurth, M. Rowen, Linac Coherent Light Source soft x-ray materials science instrument optical design and monochromator commissioning. *Rev. Sci. Instrum.* 82, 093104 (2011).

[58] M. H. Seaberg, B. Holladay, J. C. T. Lee, M. Sikorski, A. H. Reid, S. A. Montoya, G. L. Dakovski, J. D. Koralek, G. Coslovich, S. Moeller, others, Nanosecond x-ray photon correlation spectroscopy on magnetic skyrmions. *Phys. Rev. Lett.* 119, 67403 (2017).

[59] J. Chalupsky, P. Bohacek, V. Hajkova, S. P. Hau-Riege, P. A. Heimann, L. Juha, J. Krzywinski, M. Messerschmidt, S. P. Moeller, B. Nagler, M. Rowen, W. F. Schlotter, M. L. Swiggers, J. J. Turner, Comparing different approaches to characterization of focused X-ray laser beams. *Nucl. Instruments Methods Phys. Res. Sect. A Accel. Spectrometers, Detect. Assoc. Equip.* 631, 130–133 (2011).

[60] S. O. Hruszkewycz, M. Sutton, P. H. Fuoss, B. Adams, S. Rosenkranz, K. F. Ludwig Jr, W. Roseker, D. Fritz, M. Cammarata, D. Zhu, others, Supplemental Material for" High Contrast X-ray Speckle from Atomic-Scale Order in Liquids and Glasses". *arXiv Prepr. arXiv1207.2487* (2012).

[61] C. DeCaro, V. N. Karunaratne, S. Bera, L. B. Lurio, A. R. Sandy, S. Narayanan, M. Sutton, J. Winans, K. Duffin, J. Lehuta, N. Karonis, IUCr, X-ray speckle visibility spectroscopy in the single-photon limit. *J. Synchrotron Radiat.* 20, 332–338 (2013).

[62] L. J. Bannenberg, K. Kakurai, P. Falus, E. Lelièvre-Berna, R. Dalgliesh, C. D. Dewhurst, F. Qian, Y. Onose, Y. Endoh, Y. Tokura, others, Universality of the helimagnetic transition in cubic chiral magnets: Small angle neutron scattering and neutron spin echo spectroscopy studies of FeCoSi. *Phys. Rev. B.* 95, 144433 (2017).

[63] X. Lu, S. G. J. Mochrie, S. Narayanan, A. R. Sandy, M. Sprung, How a Liquid Becomes a Glass Both on Cooling and on Heating. *Phys. Rev. Lett.* 100, 045701 (2008).

[64] L. Cipelletti, L. Ramos, S. Manley, E. Pitard, D. A. Weitz, E. E. Pashkovski, M. Johansson, Universal non-diffusive slow dynamics in aging soft matter. *Faraday Discuss.* 123, 237–251 (2003).

[65] P. Chaudhuri, L. Berthier, W. Kob, Universal Nature of Particle Displacements close to Glass and Jamming Transitions. *Phys. Rev. Lett.* 99, 060604 (2007).

[66] X. Li, D. Hui, X. Lai, Battery Energy Storage Station (BESS)-Based Smoothing Control of Photovoltaic (PV) and Wind Power Generation Fluctuations. *IEEE Trans. Sustain.*

Energy. 4, 464–473 (2013).

[67] E. M. Erickson, C. Ghanty, D. Aurbach, New Horizons for Conventional Lithium Ion Battery Technology. *J. Phys. Chem. Lett.* 5, 3313–3324 (2014).

[68] M. Yoshio, R. J. Brodd, A. Kozawa, *Lithium-ion batteries* (Springer, 2009), vol. 1.

[69] A. Jossen, Fundamentals of battery dynamics. *J. Power Sources*. 154, 530–538 (2006).

[70] P. B. Balbuena, Y. Wang, *Lithium-Ion Batteries* (Imperial College Press, 2004; https://www.worldscientific.com/worldscibooks/10.1142/p291).

[71] Z. Li, J. Huang, B. Yann Liaw, V. Metzler, J. Zhang, A review of lithium deposition in lithium-ion and lithium metal secondary batteries. *J. Power Sources*. 254, 168–182 (2014).

[72] D. Aurbach, Y. Talyosef, B. Markovsky, E. Markevich, E. Zinigrad, L. Asraf, J. S. Gnanaraj, H.-J. Kim, Design of electrolyte solutions for Li and Li-ion batteries: a review. *Electrochim. Acta*. 50, 247–254 (2004).

[73] C. L. Campion, W. Li, W. B. Euler, B. L. Lucht, B. Ravdel, J. F. DiCarlo, R. Gitzendanner, K. M. Abraham, Suppression of Toxic Compounds Produced in the Decomposition of Lithium-Ion Battery Electrolytes. *Electrochem. Solid-State Lett.* 7, A194 (2004).

[74] D. H. Doughty, E. P. Roth, A General Discussion of Li Ion Battery Safety. *Interface Mag.* 21, 37–44 (2012).

[75] L. Lu, X. Han, J. Li, J. Hua, M. Ouyang, A review on the key issues for lithium-ion battery management in electric vehicles. *J. Power Sources*. 226, 272–288 (2013).

[76] Q. Wang, P. Ping, X. Zhao, G. Chu, J. Sun, C. Chen, Thermal runaway caused fire and explosion of lithium ion battery. *J. Power Sources*. 208, 210–224 (2012).

[77] S. Kalnaus, A. S. Sabau, W. E. Tenhaeff, N. J. Dudney, C. Daniel, Design of composite polymer electrolytes for Li ion batteries based on mechanical stability criteria. *J. Power Sources*. 201, 280–287 (2012).

[78] P. V Wright, Polymer electrolytes—the early days. *Electrochim. Acta*. 43, 1137–1143 (1998).

[79] W. H. Meyer, Polymer Electrolytes for Lithium-Ion Batteries. *Adv. Mater.* 10, 439–448 (1998).

[80] B. Scrosati, New approaches to developing lithium polymer batteries. *Chem. Rec.* 1, 173–181 (2001).

[81] G. Mao, M. L. Saboungi, D. L. Price, M. B. Armand, W. S. Howells, Structure of liquid

PEO-LiTFSI electrolyte. *Phys. Rev. Lett.* 84, 5536–5539 (2000).

[82] L. Edman, M. M. Doeff, A. Ferry, J. Kerr, L. C. De Jonghe, Transport Properties of the Solid Polymer Electrolyte System P(EO)nLiTFSI. *J. Phys. Chem. B*. 104, 3476–3480 (2000).

[83] O. Borodin, G. D. Smith, Mechanism of Ion Transport in Amorphous Poly(ethylene oxide)/LiTFSI from Molecular Dynamics Simulations. *Macromolecules*. 39, 1620–1629 (2006).

[84] W. Gorecki, M. Jeannin, E. Belorizky, C. Roux, M. Armand, Physical properties of solid polymer electrolyte PEO(LiTFSI) complexes. *J. Phys. Condens. Matter*. 7, 6823–6832 (1995).

[85] R. Bouchet, S. Lascaud, M. Rosso, An EIS Study of the Anode Li/PEO-LiTFSI of a Li Polymer Battery. *J. Electrochem. Soc.* 150, A1385--A1389 (2003).

[86] J.-H. Shin, W. A. Henderson, S. Passerini, Ionic liquids to the rescue? Overcoming the ionic conductivity limitations of polymer electrolytes. *Electrochem. commun.* 5, 1016–1020 (2003).

[87] J. W. Choi, G. Cheruvally, Y. H. Kim, J. K. Kim, J. Manuel, P. Raghavan, J. H. Ahn, K. W. Kim, H. J. Ahn, D. S. Choi, C. E. Song, Poly(ethylene oxide)-based polymer electrolyte incorporating room-temperature ionic liquid for lithium batteries. *Solid State Ionics*. 178, 1235–1241 (2007).

[88] Z. Xue, D. He, X. Xie, Poly(ethylene oxide)-based electrolytes for lithium-ion batteries. *J. Mater. Chem. A*. 3, 19218–19253 (2015).

[89] Y. Jiang, X. Yan, Z. Ma, P. Mei, W. Xiao, Q. You, Y. Zhang, Development of the peo based solid polymer electrolytes for all-solid state lithium ion batteries. *Polymers (Basel).* 10, 1237 (2018).

[90] W. G. Wieczorek, D. Raducha, A. Zalewska, J. R. Stevens, Effect of Salt Concentration on the Conductivity of PEO-Based Composite Polymeric Electrolytes. *J. Phys. Chem. B*. 102, 8725–8731 (1998).

[91] Z. Gadjourova, Y. G. Andreev, D. P. Tunstall, P. G. Bruce, Ionic conductivity in crystalline polymer electrolytes. *Nature*. 412, 520–523 (2001).

[92] A. A. Teran, M. H. Tang, S. A. Mullin, N. P. Balsara, Effect of molecular weight on conductivity of polymer electrolytes. *Solid State Ionics*. 203, 18–21 (2011).

[93] A. M. Christie, S. J. Lilley, E. Staunton, Y. G. Andreev, P. G. Bruce, Increasing the conductivity of crystalline polymer electrolytes. *Nature*. 433, 50–53 (2005).

[94] D. Marmorstein, T. H. Yu, K. A. Striebel, F. R. McLarnon, J. Hou, E. J. Cairns, Electrochemical performance of lithium/sulfur cells with three different polymer

electrolytes. *J. Power Sources*. 89, 219–226 (2000).

[95] A. R. Polu, H.-W. Rhee, Nanocomposite solid polymer electrolytes based on poly (ethylene oxide)/POSS-PEG (n= 13.3) hybrid nanoparticles for lithium ion batteries. *J. Ind. Eng. Chem.* 31, 323–329 (2015).

[96] F. Deng, X. Wang, D. He, J. Hu, C. Gong, Y. S. Ye, X. Xie, Z. Xue, Microporous polymer electrolyte based on PVDF/PEO star polymer blends for lithium ion batteries. *J. Memb. Sci.* 491, 82–89 (2015).

[97] J. Shi, C. A. Vincent, The effect of molecular weight on cation mobility in polymer electrolytes. *Solid State Ionics*. 60, 11–17 (1993).

[98] Z. Stoeva, I. Martin-Litas, E. Staunton, Y. G. Andreev, P. G. Bruce, Ionic Conductivity in the Crystalline Polymer Electrolytes PEO6:LiXF6, X = P, As, Sb. *J. Am. Chem. Soc.* 125, 4619–4626 (2003).

[99] S. D. Druger, M. A. Ratner, A. Nitzan, Generalized hopping model for frequency-dependent transport in a dynamically disordered medium, with applications to polymer solid electrolytes. *Phys. Rev. B*. 31, 3939–3947 (1985).

[100] A. Nitzan, M. A. Ratner, Conduction in Polymers: Dynamic Disorder Transport. *J. Phys. Chem.* 98, 1765–1775 (1994).

[101] O. Buriez, Y. B. Han, J. Hou, J. B. Kerr, J. Qiao, S. E. Sloop, M. Tian, S. Wang, Performance limitations of polymer electrolytes based on ethylene oxide polymers. *J. Power Sources*. 89, 149–155 (2000).

[102] D. T. Hallinan, N. P. Balsara, Polymer Electrolytes. *Annu. Rev. Mater. Res*. 43, 503–525 (2013).

[103] B. Scrosati, F. Croce, L. Persi, Impedance Spectroscopy Study of PEO-Based Nanocomposite Polymer Electrolytes. *J. Electrochem. Soc.* 147, 1718 (2000).

[104] Y.-T. Kim, E. S. Smotkin, The effect of plasticizers on transport and electrochemical properties of PEO-based electrolytes for lithium rechargeable batteries. *Solid State Ionics*. 149, 29–37 (2002).

[105] A. . Bloise, J. . Donoso, C. . Magon, A. . Rosario, E. . Pereira, NMR and conductivity study of PEO-based composite polymer electrolytes. *Electrochim. Acta*. 48, 2239–2246 (2003).

[106] A. Ehrl, J. Landesfeind, W. A. Wall, H. A. Gasteiger, Determination of Transport Parameters in Liquid Binary Lithium Ion Battery Electrolytes. *J. Electrochem. Soc.* 164, A826--A836 (2017).

[107] M. . Doeff, L. Edman, S. . Sloop, J. Kerr, L. . De Jonghe, Transport properties of binary salt polymer electrolytes. *J. Power Sources*. 89, 227–231 (2000).

[108] Y. Ma, M. Doyle, T. F. Fuller, M. M. Doeff, L. C. De Jonghe, J. Newman, The Measurement of a Complete Set of Transport Properties for a Concentrated Solid Polymer Electrolyte Solution. *J. Electrochem. Soc.* 142, 1859 (1995).

[109] J. Mindemark, M. J. Lacey, T. Bowden, D. Brandell, Beyond PEO—Alternative host materials for Li+-conducting solid polymer electrolytes. *Prog. Polym. Sci.* 81, 114–143 (2018).

[110] J. S. Newman, K. E. Thomas-Alyea, *Electrochemical systems* (2012).

[111] C. Gutt, T. Ghaderi, V. Chamard, A. Madsen, T. Seydel, M. Tolan, M. Sprung, G. Grübel, S. K. Sinha, Observation of Heterodyne Mixing in Surface X-Ray Photon Correlation Spectroscopy Experiments. *Phys. Rev. Lett.* 91, 076104 (2003).

[112] J. R. M. Lhermitte, M. C. Rogers, S. Manet, M. Sutton, Velocity measurement by coherent x-ray heterodyning. *Rev. Sci. Instrum.* 88 (2017).

[113] F. Khan, S. Narayanan, R. Sersted, N. Schwarz, A. Sandy, Distributed X-ray photon correlation spectroscopy data reduction using Hadoop *MapReduce*. *J. Synchrotron Radiat.* 25, 1135–1143 (2018).

[114] M. Doyle, T. F. Fuller, J. Newman, The importance of the lithium ion transference number in lithium/polymer cells. *Electrochim. Acta*. 39, 2073–2081 (1994).

[115] J. Evans, C. A. Vincent, P. G. Bruce, Electrochemical measurement of transference numbers in polymer electrolytes. *Polymer (Guildf).* 28, 2324–2328 (1987).

[116] J.-J. Song, R. Bhattacharya, H. Kim, J. Chang, T.-Y. Tang, H. Guo, S. K. Ghosh, Y. Yang, Z. Jiang, H. Kim, others, One-Dimensional Anomalous Diffusion of Gold Nanoparticles in a Polymer Melt. *Phys. Rev. Lett.* 122, 107802 (2019).

[117] J. Maier, Concentration Polarization of Salt-Containing Liquid Electrolytes. *Adv. Funct. Mater.* 21, 1448–1455 (2011).

[118] R. L. Gardas, J. A. P. Coutinho, Extension of the Ye and Shreeve group contribution method for density estimation of ionic liquids in a wide range of temperatures and pressures. *Fluid Phase Equilib.* 263, 26–32 (2008).